Probabilistic Fatigue Damage Localization at Unknown Temperatures

Using Guided Wave Methods

by

Kevin Hensberry

A Thesis Presented in Partial Fulfillment
of the Requirements for the Degree
Master of Science

Approved April 2013 by the
Graduate Supervisory Committee:

Aditi Chattopadhyay, Chair
Yongming Liu
Antonia Papandreou-Suppappola

ARIZONA STATE UNIVERISTY

May 2013

ABSTRACT

This research examines the current challenges of using Lamb wave interrogation methods to localize fatigue crack damage in a complex metallic structural component subjected to unknown temperatures. The goal of this work is to improve damage localization results for a structural component interrogated at an unknown temperature, by developing a probabilistic and reference-free framework for estimating Lamb wave velocities and the damage location. The methodology for damage localization at unknown temperatures includes the following key elements: i) a model that can describe the change in Lamb wave velocities with temperature; ii) the extension of an advanced time-frequency based signal processing technique for enhanced time-of-flight feature extraction from a dispersive signal; iii) the development of a Bayesian damage localization framework incorporating data association and sensor fusion. The technique requires no additional transducers to be installed on a structure, and allows for the estimation of both the temperature and the wave velocity in the component. Additionally, the framework of the algorithm allows it to function completely in an unsupervised manner by probabilistically accounting for all measurement origin uncertainty.

The novel algorithm was experimentally validated using an aluminum lug joint with a growing fatigue crack. The lug joint was interrogated using piezoelectric transducers at multiple fatigue crack lengths, and at temperatures between 20°C and 80°C. The results showed that the algorithm could accurately predict the temperature and wave speed of the lug joint. The localization results for the fatigue damage were found to correlate well with the true locations at long crack lengths, but loss of accuracy was observed in localizing small cracks due to time-of-flight measurement errors. To validate the algorithm across a

wider range of temperatures the electromechanically coupled LISA/SIM model was used to simulate the effects of temperatures. The numerical results showed that this approach would be capable of experimentally estimating the temperature and velocity in the lug joint for temperatures from -60°C to 150°C. The velocity estimation algorithm was found to significantly increase the accuracy of localization at temperatures above 120°C when error due to incorrect velocity selection begins to outweigh the error due to time-of-flight measurements.

ACKNOWLEDGMENTS

I would first like to thank Dr. Aditi Chattopadhyay for giving me the opportunity to work in her research group. Without her support, I would have never been able to finish my research. I would also like to thank my committee members, Dr. Yongming Liu and Dr. Antonia Papandreou-Suppappola, for all of their support in completing this thesis.

I am most thankful for all of the support that I have received from the other members of the research group including Dr. Albert Moncada, Dr. Masoud Yekani Fard, Dr. Yingtao Liu, Anthony Vizzini, Bonsung Koo, Inho Kim, Jinjun Zhang, Joel Johnston, Luke Borkowski, Rajesh Neerukatti, Ryan Lawson, and Scott Leemans. I would especially like to thank Dr. K.C. Liu and Dr. Narayan Kovvali for all of their help and guidance in making this research possible.

My family and friends were invaluable throughout my entire grad school experience. I thank all of them for putting up with me as I went back and forth daily between loving and hating grad school. I also could have never accomplished any of this without Dr. David Lanning from Embry-Riddle who encouraged me to pursue a graduate degree.

Finally, I would like to thank Dr. David Stargel and the Air Force Office of Scientific Research's Multidisciplinary University Research Initiative Grant, FA95550-06-1-0309 for supporting this research.

TABLE OF CONTENTS

Page

CHAPTER Page

LIST OF TABLES

LIST OF FIGURES

Figure Page

Figure Page

Chapter 1

INTRODUCTION

As aerospace vehicles are pushed towards their material and structural limits, new and more sophisticated techniques need to be developed to assess the integrity of the system. Currently, assessment of a structure's health is conducted by a variety of nondestructive evaluation (NDE) techniques. These techniques require a structural component to be taken out of service at specific intervals and be inspected for signs of damage. Current NDE techniques include the use of ultrasonic testing, flash thermography, magnetic particle, eddy current, radiography, and liquid penetrant [1]. These specific techniques have all been proven to provide accurate estimates of damage; however, none of the techniques can provide information on the presence or size of damage while the structure is in service.

In order to obtain information about the health of a structure in real time a structural health monitoring (SHM) framework is needed. The overall objective of an SHM system is to monitor a structure in real time, detect if damage is present, localize and characterize the damage, generate a prognosis for the structure, and determine if the structure is safe to operate. With the availability of a real-time measure of an aerospace vehicle's health, the safety and reliability of the system is increased from current standards. By implementing an SHM system the aerospace industry can move away from a schedule based maintenance (SBM) to condition based maintenance (CBM) inspection routine. Moving towards a CBM program will allow aircraft operators to see a large reduction in their operating costs because an aircraft is removed from service less often than with the traditional SBM

program. The benefits described for an SHM system with a CBM program are not only for the aerospace industry, but also for civil infrastructure and other mechanical systems.

There are many challenges involved in implementing an SHM system. One of the primary concerns in the aerospace industry is that of additional weight penalty. Currently, there are few SHM systems installed on aircraft; this means that adding a new SHM system will either require weight to be removed from other components, or require a reduction in the performance of the aircraft. To implement an SHM system a dispersed sensor network is required to collect information across the structure. The sensor placement must be optimized in order to collect the data necessary for detection and localization with the fewest number of sensors [2]. After the data is collected it must be transmitted back to a computer that can evaluate the data for information on the health of the structure. Obviously, there is a weight penalty with the additional sensors and computing power. To offset the sensor weight penalty there is research being done on the use of many small light-weight sensors such as piezoelectric transducers, macro fiber composites, and fiber Bragg gratings [3]. Other SHM research includes investigating the wireless transmission of data from the sensor network to a central computer in order to decrease the overall SHM system weight [4].

A major challenge in SHM is the lack of robust techniques to detect, localize, characterize, and predict damage. Many of the current techniques are capable of achieving these goals in laboratory conditions, but have deteriorated performance in an actual operating environment. For damage localization many techniques use guided waves to determine the location of damage, and rely heavily on baseline data. Once a structural component is exposed to operating conditions, which may include a variety of

environments, these baseline signals change, and the localization techniques begin to provide poor results.

The next sections briefly explain how a distributed network of sensors can localize damage in a structure using elastic wave propagation. Then an overview of the methods currently available to localize damage and analyze sensor data will be presented. Finally, the objectives and novel contributions of this work will be summarized.

1.1. Fundamentals of Elastic Wave Propagation

Lamb waves are one of the standard types of guided waves that are used for wave propagation in an SHM system. Lamb waves were first characterized by Horace Lamb in 1917. In Lamb's original work he derived the equations necessary to describe waves propagating in homogeneous, isotropic, flat plates [5]. Lamb waves are popular for SHM systems because they have very low attenuation, allowing the waves to travel long distances in thin structures such as the skin of an aircraft. This allows Lamb waves to interrogate difficult to reach locations for possible damage.

A complete derivation of the Lamb wave equation is presented by Graff [6]. In this approach there is the assumption of a plane strain system of waves propagating in a plate of thickness 2*d* with traction free boundary conditions. By solving the elastodynamic wave equation for these conditions, the generalized Rayleigh-Lamb frequency equation can be found as

$$\frac{\tan(\beta d)}{\tan(\alpha d)} = -\left(\frac{4\xi^2 \alpha\beta}{\left(\xi^2 - \beta^2\right)^2} \right)^{\pm 1}, \tag{1.1}$$

where +1 and -1 refer to symmetric and antisymmetric motion respectively, and ξ, α, and β are defined as

$$\xi^2 = \frac{\omega^2}{c^2}, \tag{1.2}$$

$$\alpha^2 = \frac{\omega^2}{c_p^2} - \xi^2, \tag{1.3}$$

$$\beta^2 = \frac{\omega^2}{c_s^2} - \xi^2. \tag{1.4}$$

In equations (1.2) through (1.4) ω is the frequency, c is the wave speed, c_p is the primary wave speed, and c_s is the secondary wave speed. By examining these equations it is clear that there is a relationship between the wave speed and the frequency that causes Lamb waves to be dispersive. When waves are dispersive it is important to define the relationship between phase velocity and group velocity. The group velocity c_g can be defined as

$$c_g = c - \lambda \frac{\partial c}{\partial \lambda}, \tag{1.5}$$

where λ is the wavelength of the propagating wave, and c is the wave velocity. The physical difference between group and phase velocity is that group velocity is the velocity at which a wave packet travels, while the phase velocity is the velocity at which the phase of the wave travels. For damage localization the group velocity is used because it refers to the physical propagation of the entire wave packet.

By solving the Rayleigh-Lamb frequency equation, the dispersion curves for the Lamb waves are obtained. Dispersion curves relate the group and phase velocity to the frequency-thickness of the propagating wave. An example of a dispersion curve can be seen in Figure 1.1.

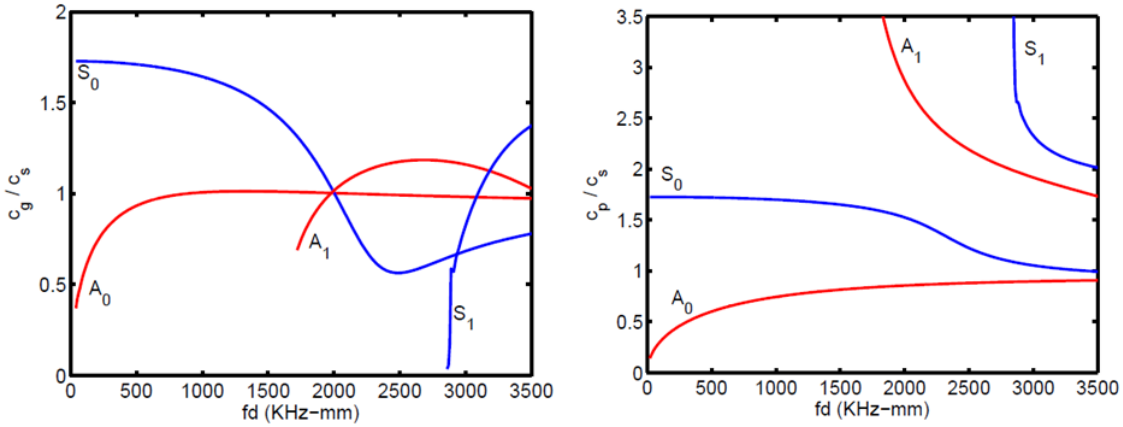

Figure 1.1. Example dispersion curves.

Figure 1.1 shows how the velocities of the symmetric and antisymmetric modes propagating through a plate vary with frequency. Also shown in Figure 1.1 are the higher order modes A_1 and S_1. These higher order modes exist because the Rayleigh-Lamb frequency equation is a transcendental equation.

1.2. Damage Localization

Using the results of the Rayleigh-Lamb frequency equation, Eqn. (1.1), a formulation can be derived for the localization of damage in an isotropic plate. Assuming isotropic wave propagation, the time-of-flight of a wave from an actuator, to a damage, and to a sensor can be defined as

$$\tau = \frac{\sqrt{(x_a - x_d)^2 + (y_a - y_d)^2}}{v_1} + \frac{\sqrt{(x_s - x_d)^2 + (y_s - y_d)^2}}{v_2}, \tag{1.6}$$

where τ is the time-of-flight, (x_a,y_a) is the actuator location, (x_d,y_d) is the damage location, (x_s,y_s) is the sensor location, v_1 is the group velocity from the actuator to the damage, and v_2 is the group velocity from the damage to the sensor. If no mode conversion is assumed v_1 and v_2 are considered equal. An ellipse of possible damage locations can be formed with

the foci as the actuator and sensor positions by using Eqn. (1.6) with a fixed value for the actuator and sensor positions, velocity, and τ.

Typically, a single actuator-sensor pair, or sensor path, is insufficient to localize damage, so an array of sensor paths is required. Using Eqn. (1.6) for each sensor path, an elliptical solution of possible damage locations for each sensor path can be obtained. Ideally, the ellipses from every sensor path will intersect at one exact point indicating the true damage position. However, there is typically no unique solution for the damage location due to errors in the time-of-flight measurements during experiments. In order to predict a unique damage location in this situation an estimator, such as the least squares estimate, must be used. Soni at al. [7] presented a methodology to localize a fatigue crack tip using this type of triangulation method. The method (using three sensors) utilized the mode conversion from the crack tip to localize the damage. The procedure was then used to estimate the crack length and provided excellent results at lengths greater than 9 mm.

Most localization techniques use a baseline signal to aid in localization. Typically, a baseline signal is collected when the structure is in a known or healthy state. This baseline signal is then subtracted from any signal obtained once the structure is in service. If the difference between the two signals is small, and below a predefined threshold, it can be concluded that no damage is present in the structure. If there is a large difference in the two signals the residual signal can be used to localize damage using techniques such as time-of-arrival imaging, time-difference-of-arrival imaging, or the energy arrival imaging method [8, 9]. While all of these techniques have been shown to localize damage well, they rely heavily on the baseline signal. If the baseline signal changes, or is no longer representative of the healthy structure, localization error increases dramatically and so do the number of

false alarms for damage detection. Baseline-free techniques can eliminate the limitations of adaptability with a changing environment.

An interesting technique developed to detect and localize damage without the use of baseline signals uses boundary reflection compensation and adaptive source removal [10, 11]. This method uses virtual sources to model the boundaries of a structure, and models the wave propagation due to the actuation signal using a dispersion model. By combining the results from the virtual sources and dispersed actuation signal, a theoretical baseline can be developed. This theoretical baseline can then be adaptively scaled and shifted in order to fit the actual signals received from the experiment. After the theoretical baseline is calculated, the difference between the signals is taken and the localization is conducted using one of the previously mentioned techniques. This technique has been shown to have significantly more artifacts in the final image than those that use true baseline signals. If a theoretical baseline is to be utilized, a more representative model for how a wave disperses and interacts with boundaries must be used.

Obviously, a large amount of information is being discarded when these elliptical solutions provide only a point solution, or a deterministic estimate. One of the major drawbacks of these deterministic techniques is that there is no quantification of error. With no quantification of the accumulated error, there is no quantitative parameter that can be examined to determine the accuracy of the localization result. These major limitations have caused researchers to investigate probabilistic methods to localize damage. Probabilistic methods allow measurement errors to be included in the localization, this allows for a high probability region of the damage location to be defined.

Within the category of probabilistic localization algorithms there are those that use baseline signals and those that do not. The use of the baseline signal is, again, a major limitation, even when an adaptive algorithm is used to shift and scale the baseline to match the experimental signal. One baseline technique which has been shown to localize damage well is the Rayleigh maximum-likelihood estimate (RMLE) method. This method derives a maximum-likelihood estimator by assuming a Rayleigh distribution as the likelihood function for the damage location. This method was found to have slightly better performance than most deterministic localization algorithms, the exception being the energy arrival method [12]. The RMLE was later modified using Bayesian statistics. By including *a priori* information the damage estimation accuracy increased. It was also shown that this algorithm was more capable of accounting for incorrect placement of the sensors than the deterministic algorithms [13].

One of the first fully probabilistic localization algorithms was proposed by Zhou et al [14]. In this approach, a probability value is assigned to every pixel used to image a structure utilizing a technique known as probability-based diagnostic imaging (PDI). This approach also investigated both fusing images from all sensors, and fusing images from different interrogation techniques such as pulse-echo and pitch-catch. The algorithm was later extended to account for wave attenuation, and was used to investigate flaws oriented at various angles [15]. Additional sensor fusion techniques (such as the disjunctive, conjunctive, and compromise methods) were later investigated using Zhou's probabilistic approach [16]. To create a complete probabilistic damage detection and localization algorithm, Yu added a kernel density estimation detection algorithm to Zhou's localization algorithm [17].

The next major improvement in probabilistic localization methods came with the use of the extended Kalman filter (EKF). The EKF approach, presented by Niri et al. [18], was proposed to locate an acoustic emission source and identify the wave speed. The approach considered both the time-of-flight and the wave speed as Gaussian random variables, and accounted for systematic error in the time-of-flight measurements due to Heisenberg uncertainty [18]. This technique was later extended to account for random errors due to environmental noise [19]. Adaptive sensor selection and sensor weighting was also added in the extended technique [20]. By adding sensor selection and weighting, only the most reliable information related to the acoustic emission source would be considered in the EKF algorithm.

A recent advancement in probabilistic damage localization is due to Yan [21]. Yan proposed a Bayesian technique to combine prior information with time-of-flight data. The Markov chain Monte Carlo (MCMC) method was used to estimate both the wave speed and the damage location. Yan's method assumes that uncertainty in the time-of-flight data can be modeled using two independent Gaussian variables representing modeling error and measurement uncertainty. This method was shown, both numerically and experimentally, to estimate both the wave speed and the damage location accurately. The major limitation of this approach is in the computational cost of the MCMC method. In the algorithm validation the MCMC method required 100,000 samples to estimate each parameter, which causes this algorithm to be one of the most computationally expensive algorithms.

1.3. Signal Processing in Structural Health Monitoring

Advanced signal processing techniques are critical components of an SHM framework. Typically, information about a structure is obtained from transducers that

provide electrical signals, which correspond to the mechanical response of the structure. For wave-based SHM, an interrogating device must be capable of both actuating and sensing in order to reduce the weight and cost of the system. Devices that are capable of this (and that are currently used) include lead zirconate titante (PZT) piezoelectric transducers, macro fiber composites (MFCs), and fiber Bragg grating sensors (FBGs). Throughout this investigation PZT transducers will be used due to their low weight, small size, and low cost, which makes them ideal for use in aerospace applications.

Many different techniques have been proposed for signal processing in SHM systems. For damage localization, the goal of signal processing is to extract an accurate estimate of a wave's time-of-flight. Difficulties occur in extracting accurate time-of-flights because the wave modes can be highly dispersive, and there can be multiple waves arriving at the same time causing destructive interference. These inherent issues from guided waves cause problems in traditional signal processing techniques that function solely in the time domain, so advanced time-frequency analysis techniques must be used. Xu et al. investigated the differences between the cross correlation [22], envelope moment [23], dispersion compensation [24], and matching pursuit decomposition techniques [25]. The authors found that the time domain techniques of cross correlation and envelope moment had the largest amount of error when decomposing an experimental signal. Matching pursuit and dispersion compensation were found to have similar performance; however, dispersion compensation could only properly decompose single-mode waves [26]. Due to the conclusion that time-frequency techniques can more accurately estimate time-of-flight, a large amount of research has gone into their use. Since time-frequency based techniques

are found to provide better results, a significant amount of work has been reported in developing these algorithms.

Two of the most popular time-frequency techniques are continuous wavelet transform (CWT) [27] and matching pursuit decomposition (MPD) [25]. The CWT algorithm decomposes a signal by matching shifted and scaled wavelets to the real signal using the inner product. The shifting and scaling of the wavelets causes an increase in the time or frequency resolution, but a decrease in the other. The CWT algorithm has been successfully used in SHM for time-of-flight extraction [18, 21, 28, 29], and damage detection [30]. In contrast, MPD decomposes a signal by finding a linear expansion of weighted basis functions. The basis functions are found from an over-defined dictionary and are matched to the signal using the inner product. The MPD framework allows the MPD algorithm to gain better time and frequency resolution than the CWT. In SHM applications, the MPD algorithm has been used to decompose Lamb wave modes [31-33], detect fatigue damage [34, 35], and detect composite delamination [36]. Both time-frequency techniques produce a representation of the original signal in the time-frequency domain, allowing for a more accurate characterization of the dispersive wave modes.

Many other advanced techniques have been developed for feature extraction of guided wave signals. For dispersive signals, Okopal et al. developed a feature known as an attenuation and dispersion-invariant moment. This feature was experimentally shown to outperform ordinary temporal moments and correlation coefficients in water [37, 38]. By using dispersion invariant features such as this, additional parameters can be used to characterize guided waves in the detection, localization, and characterization portions of the SHM framework. Another technique to limit the effects of dispersion is presented by

Wilcox. Wilcox's approach uses knowledge of the dispersion curves for the material to account for the effects of dispersion. This technique allows for a received dispersive signal to be backwards propagated, allowing for the easier analysis of a nondispersive signal [39]. Time reversal techniques are similar to the technique of Wilcox. Time reversal takes a signal actuated by A and received by B, reverses the signal received by B in time, and actuates the reversed signal from B. The signal received by A can again be time reversed and compared to the original signal [40, 41]. By comparing the original and time reversed signals the health of the structure can be quantified. Hoseini et al. [42] developed a probabilistic framework for time-of-flight extraction using a quasi-maximum likelihood method to estimate the parameters of a Gaussian envelope model. The quasi maximum likelihood method was experimentally found to increase time-of-flight accuracy compared to the results from a cross correlation analysis. Flynn also proposed a probabilistic technique that uses low-order stochastic modeling to more accurately extract critical features [43].

1.4. Effects of Temperature on Elastic Waves

As temperature increases the effects of the thermal loads on a structure can no longer be ignored. A complete summary of the thermo-mechanical effects on elastic wave propagation was studied by Francis [44]. The largest impact that temperature has on Lamb wave propagation is due to changes in the elastic properties of the material. Changing material properties requires the Lamb wave dispersion curves to be recalculated for a variety of temperatures. Gandhi et al. [45] presented an efficient perturbation analysis for calculating Lamb wave dispersion curves at different temperatures. Exact knowledge of the

dispersion curves is required for damage localization because localization error will increase dramatically if the true wave speed is not used.

Raghavan et al. [46] completed one of the most complete reviews on the effects of elevated temperature on guided wave SHM. They investigated the effects of thermal loading on the adhesive layers used to attach sensors, temperature effects on the differences between baseline and actual signals, and temperature effects on damage characterization. The most important information obtained from this study was the relative sensitivity of material parameters to thermal loads. The authors also showed that the changes in the elastic modulus of the structure were significant, while the effect on the moduli of the PZT sensors was relatively small. The piezoelectric properties of the sensors were also shown to be significantly affected by elevated temperature. However, changes due to the thermal expansion and in the structural damping were found to be minimal, and were not thought to cause large effects on the guided wave SHM system.

Temperature increase also affects material properties. A variety of techniques have been developed to account for this effect. Many of the previous damage localization algorithms relied on baseline signals to assess the structure's health. When a baseline signal taken at room temperature is compared to a baseline signal taken at an elevated temperature, significant differences are observed. The primary effect of temperature is to shift and scale a signal in the time domain. To account for these effects a technique called Optimal Baseline Subtraction (OBS) and Baseline Signal Stretch (BSS) have been developed [47-51]. These methods compare a received signal to a database of baselines, which were collected at various environmental conditions and temperatures. The baseline with which the collected signal correlates best is then shifted and scaled to achieve a higher

correlation with the collected signal. The difference between the collected signal and its stretched optimal baseline is then computed. Damage localization then continues in the same manner as the previously described localization methods.

As with damage localization at room temperature, methods that use baselines are not ideal due to their inherent errors from measurements and the environment. For damage localization at elevated temperatures it is common to assume that changes in wave speed lead to the only first order effects on localization error. Due to this assumption, a localization approach which can estimate the true wave speed, or is independent of wave speed, is ideal. The probabilistic methods already presented by Niri [18-20] and Yan [21] have the ideal feature of estimating the wave speed from the time-of-flight measurements. Moll et al. [52] presented a novel approach, which was completely independent of group velocity information. The approach uses sensor triplets, which consist of two actuators and one receiver. By using simple geometric principles damage can be localized using a spatially dispersed array of sensors. This algorithm was experimentally shown to be capable of localizing damage in both isotropic and quasi-isotropic plates, but required a large number of sensors.

1.5. Objectives

The objective of this research is to develop a probabilistic methodology to localize fatigue damage in a geometrically-complex metallic structure at an unknown temperature using guided wave methods. The overall objective comprises three research tasks: (i) develop a novel time-frequency analysis signal processing algorithm that can increase the accuracy of the time-of-flight estimations of a dispersive wave signal; (ii) develop a fully probabilistic damage localization algorithm that can account for uncertainty in the time-of-

flight measurements; (iii) develop a probabilistic method capable of estimating temperature and wave speed, which can be used to improve damage localization results at elevated or unknown temperatures.

The methodologies developed to address the first two tasks are discussed in Chapter 2. First, the grouped matching pursuit decomposition method is presented which allows computationally-simple atoms to decompose a signal and later be combined into dispersive modes to increase the time-of-flight estimation accuracy. Next, a probabilistic framework for damage localization is presented. Within the probabilistic framework is an algorithm called probabilistic data association [53-55]. Data association allows the localization framework to account for the uncertainty in the time-of-flight measurements, and allows the entire localization algorithm to function in an unsupervised manner. Finally, experimental validation of the proposed grouped MPD and probabilistic localization framework is conducted on an aluminum lug joint with a growing fatigue crack.

Chapter 3 details the framework for temperature and velocity estimation. First, a summary of how temperature affects the Lamb wave dispersion curves is presented. Second, using the information on how wave velocity changes with temperature a temperature-velocity dictionary is created. Third, the algorithm used to estimate temperature and velocity is explained, along with how it can be incorporated with the localization algorithm. Fourth, experimental validation is completed by first showing that the algorithm can predict temperature and wave speed, and then by showing the benefits obtained from using velocity estimation by localizing fatigue damage at a range of temperatures. Finally, a numerical investigation is conducted to validate the algorithm at a wider temperature range.

Chapter 2

PROBABILISTIC DAMAGE LOCALIZATION IN COMPLEX-GEOMETRY METALLIC STRUCTURES

Damage localization is one of the primary thrust areas of SHM research. Accurately localizing damage in a structure provides engineers with the critical information necessary to know when a structure is no longer safe to operate. One particular challenge in damage localization is that of creating a framework that can extract and account for the uncertainty of the critical parameters needed for localization. This chapter describes an approach to probabilistically localize damage using a combined Bayesian and probabilistic data association framework. The proposed algorithm was applied to a complex-geometry metallic structure with growing fatigue damage. The objective was to demonstrate the ability of probabilistic data association to account for measurement origin uncertainty while still accurately localizing damage. Section 2.1 provides the theoretical framework for the probabilistic damage localization framework, Section 2.2 shows the experimental validation of the proposed algorithm, and Section 2.3 provides concluding remarks on the algorithm and the results.

2.1. Probabilistic Damage Localization Algorithm

The proposed probabilistic damage localization algorithm, shown in Figure 2.1, can be summarized in the following six steps: i) Discretize the domain being interrogated; ii) Interrogate the structure using a 500 kHz actuation signal and subtract the received signals in each sensor path; iii) Decompose the differenced signal using the grouped MPD algorithm for each sensor path; iv) Extract the time-of-flights from the MPD algorithm and implement this information into the Bayesian probabilistic localization algorithm; v) Use

the validation gate to ensure time-of-flight measurement accuracy; vi) Fuse the localization results from each sensor path to create the final probabilistic damage localization result. The theoretical framework of the feature extraction and probabilistic methods used in the algorithm will be described in further detail in the following sections.

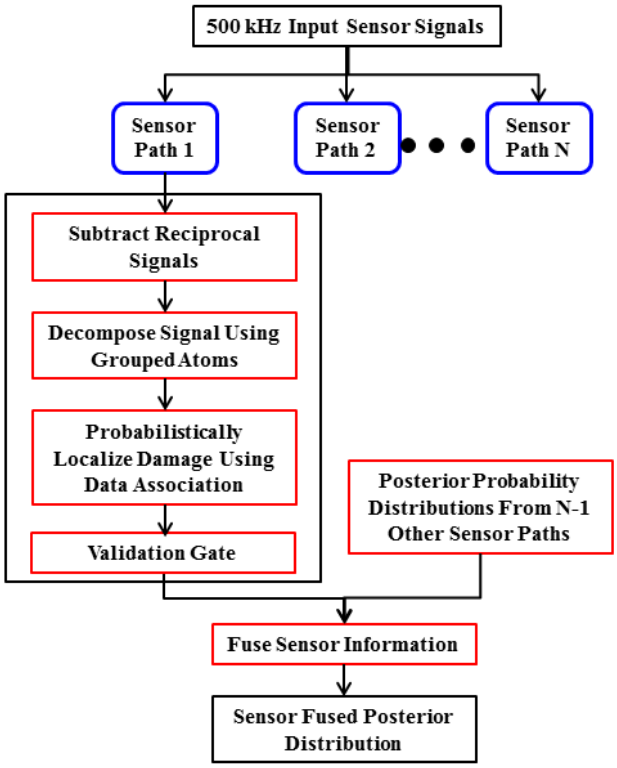

Figure 2.1. Flow chart of probabilistic localization algorithm.

2.1.1. Grouped Matching Pursuit Decomposition Feature Extraction

The MPD algorithm decomposes a signal into a weighted linear expansion of elementary basis functions, or atoms [25]. In application, the signal *x(t)* can be expressed using the MPD algorithm as

$$x(t) = \sum_{i=0}^{Z-1} \alpha_i g_i(t) + r_Z(t), \tag{2.1}$$

where α_i is the ith expansion coefficient, $g_i(t)$ is the ith basis function, and $r_Z(t)$ is the residual signal after a user set Z number of iterations. The basis functions $g_i(t)$ are chosen from a predefined set, or dictionary, such that the MPD algorithm matches and extracts the main signal components of interest and filters out the noise [7]. The MPD algorithm is an iterative algorithm, which affects the decomposition based upon the magnitude of the match (coefficient α). This sorting means that the values of α_i, which have lower values of i, correspond to the basis functions with the highest energy (best match). Formulation of basis functions that can capture the generalized dispersive shape of Lamb wave modes is nearly impossible due to dispersion. Previous work, which used the MPD algorithm to decompose Lamb wave signals, used a basis function of Gaussian time-frequency shifted and scaled harmonics of the form

$$g^{(d)}(t) = (8\kappa_l / \pi)^{1/4} e^{-\kappa_l (t-\lambda_n)^2} \cos(2\pi \upsilon_m t), \tag{2.2}$$

where $d = \lambda_n, \upsilon_m, \kappa_l$ is the set of all atoms time-shifted by λ_n (n = 1,…,N_d), frequency-shifted by ν_m (m = 1,…,M_d), and time-scaled by κ_l (l = 1,…, L_d) [7]. In order to create a dispersive (or more generally shaped) atom, many simpler Gaussian time-frequency shifted and scaled atoms can be grouped together.

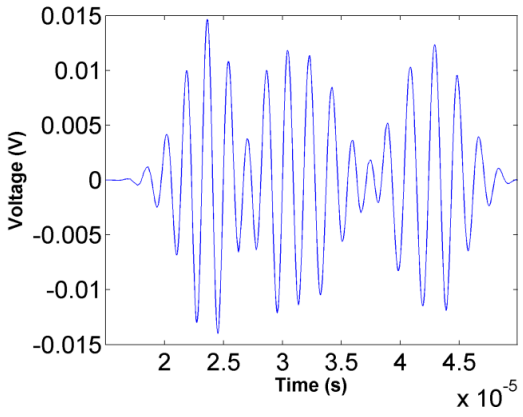

Figure 2.2. Example of a typical Lamb wave dispersive signal.

Consider a general dispersive signal as shown in Figure 2.2. The signal appears to have three dominant modes present, as seen by the three peaks in the signal. The modes are dispersive and have arbitrary shapes; thus, a single Gaussian atom for each mode would provide a poor estimate of the modes' time-of-flight. To increase the accuracy in the measured time-of-flight, the signal must be decomposed into *Z* atoms. The *Z* atoms must then be grouped to the proper mode in the signal, in order to create the dispersive modes. To group the *Z* atoms to the proper modes, the absolute value of the Hilbert transform can be used as shown in Figure 2.3 to estimate the time-of-flight of the dominant modes.

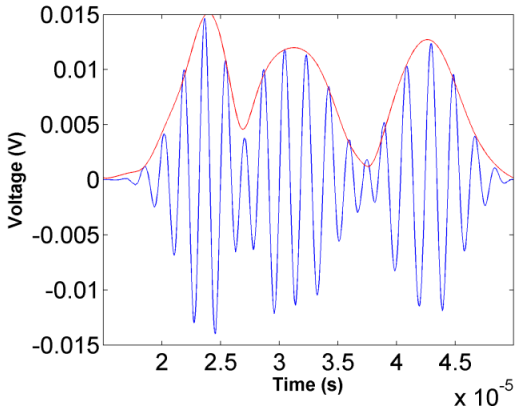

Figure 2.3. Hilbert transform of dispersive wave signal used to find number of modes present in signal.

The absolute value of the Hilbert transform creates an envelope of the wave signal as shown in red in Figure 2.3. The peaks of the envelope correspond to the approximate centers of each mode present in the signal. To improve this approximation, the MPD atoms closest to each peak in the envelope are grouped together to create a new dispersive atom. If there are K peaks in the envelope corresponding to a set of time-of-flights $\gamma = \{\gamma_1, \gamma_2, ..., \gamma_K\}$, an atom with time-of-flight t_a is grouped to the envelope peak, with which the magnitude of their difference is a minimum using the following equation.

$$\text{Dominant Mode} = \arg\min_i |t_a - \gamma_i|. \tag{2.3}$$

An example of this grouping when K=3 is shown in Figure 2.4.

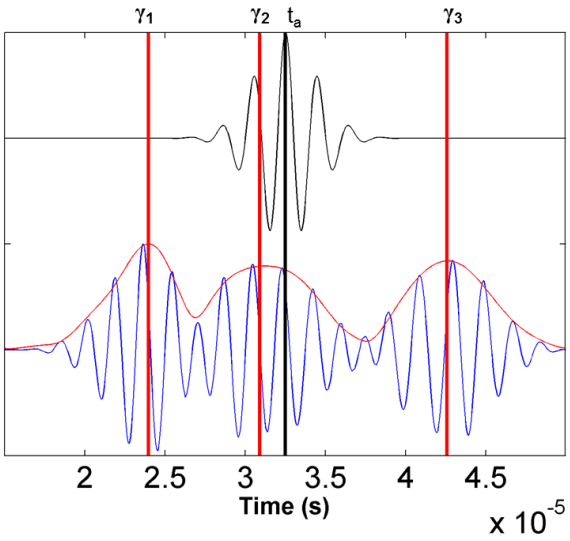

Figure 2.4. Example of grouping an MPD atom in a dispersive signal.

Figure 2.4 shows that the wave signal has three peaks with time-of-flights corresponding to γ_1, γ_2, and γ_3, and the atom has time-of-flight t_a. In this example, the minimum difference in time-of-flights is between γ_2 and t_a; therefore, the atom would be assigned to mode 2 and would be grouped with all other atoms assigned to mode 2. If this

same grouping procedure is followed for all Z atoms, K dispersive atoms will be created to represent the original wave signal as shown in Figure 2.5.

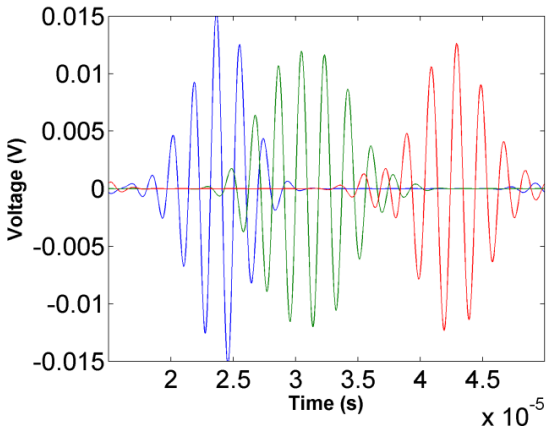

Figure 2.5. Example of MPD atoms being fully grouped to dispersive signal.

Figure 2.5 shows that simple Gaussian atoms can be combined to create dispersive, or any generally shaped mode, in a signal. To complete the grouping of the MPD atoms, the time-of-flights of every individual atom contributing to the grouped atoms must be combined to obtain an approximate time-of-flight for each of the new grouped atoms. The combination of individual time-of-flights is accomplished using the mean time-shift, defined as

$$\bar{t} = \frac{\int t\left|x(t)\right|^2 dt}{\int \left|x(t)\right|^2 dt}. \tag{2.4}$$

2.1.2. Probabilistic Damage Localization

The damage localization approach is based on the analysis of dispersive wave propagation in materials. As discussed in Section 2.1.1, time-of-flight information is first extracted from Lamb wave sensor data using the grouped matching pursuit decomposition

(MPD) algorithm [25] with a Gaussian time-frequency [56] dictionary. The extracted time-of-flight of the A_0 mode reflecting off a damage is then utilized for the localization.

The probabilistic damage localization algorithm proposed here uses a Bayesian approach; this is done to optimally combine information from prior knowledge about the damage location from physics with that from (noisy) time-of-flight measurements obtained from wave based sensor data. Let the τ denote the time-of-flight of a damage reflected wave obtained using grouped MPD from a sensor signal corresponding to damage located at (x_c, y_c). Assuming simple isotropic propagation of the wave from the transmitter to the damage, and from the damage to the receiver, τ can be written as

$$\tau = \frac{\sqrt{(x_t - x_c)^2 + (y_t - y_c)^2} + \sqrt{(x_r - x_c)^2 + (y_r - y_c)^2}}{v_{A_0}} + e. \tag{2.5}$$

In Eqn. (2.1), (x_t, y_t) and (x_r, y_r) are the respective positions of the transmitter and receiver, v_{A0} is the A_0 wave velocity, and e is the measurement noise term that models the uncertainty in the time-of-flight obtained via MPD. In this investigation, a Gaussian probability distribution was used for e:

$$e \sim \mathcal{N}(0, \sigma^2) = \frac{1}{\sqrt{2\pi}\sigma} \exp\left[-\frac{e^2}{2\sigma^2} \right], \tag{2.6}$$

with zero mean and variance σ^2. Together, Eqn. (2.5) and Eqn. (2.6) define the likelihood function for the damage location, given by

$$p(\tau \mid x_c, y_c) = \frac{1}{\sqrt{2\pi}\sigma} \exp\left[-\frac{1}{2\sigma^2} \left(\tau - \frac{\sqrt{(x_t - x_c)^2 + (y_t - y_c)^2}}{v_{A_0}} - \frac{\sqrt{(x_r - x_c)^2 + (y_r - y_c)^2}}{v_{A_0}} \right)^2 \right], \tag{2.7}$$

where the notation $p(\cdot|\cdot)$ denotes conditional probability. Using Bayes' theorem [57-59], the likelihood Eqn. (2.7) is combined with a prior probability distribution $p(x_c, y_c)$ defined

over the interrogation region $\mathcal{D}$ to obtain the posterior probability distribution of the damage location given the time-of-flight as

$$p(x_c, y_c \mid \tau) = \frac{p(\tau \mid x_c, y_c)\, p(x_c, y_c)}{\int_{\mathcal{D}} p(\tau \mid x_c, y_c)\, p(x_c, y_c) d(x_c, y_c)} \propto p(\tau \mid x_c, y_c)\, p(x_c, y_c). \tag{2.8}$$

The estimate $(\hat{x}_c, \hat{y}_c)$ of the damage location can then be computed as the mean or the mode (equivalent to the maximum) of the posterior:

$$\begin{aligned} (\hat{x}_c, \hat{y}_c)^{\text{mean}} &= E[(x_c, y_c) \mid \tau] \triangleq \int_{\mathcal{D}} (x_c, y_c)\, p(x_c, y_c \mid \tau) d(x_c, y_c), \\ (\hat{x}_c, \hat{y}_c)^{\text{mode}} &= \arg\max_{(x_c, y_c) \in \mathcal{D}} p(x_c, y_c \mid \tau), \end{aligned} \tag{2.9}$$

where $E[\cdot]$ denotes statistical expectation. The covariance of the posterior distribution, given by

$$\text{Cov}\left[(x_c, y_c) \mid \tau\right] = \int_{\mathcal{D}} \left[(x_c, y_c) - (\hat{x}_c, \hat{y}_c)\right]\left[(x_c, y_c) - (\hat{x}_c, \hat{y}_c)\right]^T p(x_c, y_c \mid \tau) d(x_c, y_c), \tag{2.10}$$

provides a measure of the uncertainty in the damage location based on the available information. In particular, the probability $p_{\mathcal{D}_s}$ that the damage is located in a sub-region $\mathcal{D}_s \subseteq \mathcal{D}$ is given by

$$p_{\mathcal{D}_s} = \int_{\mathcal{D}_s} p(x_c, y_c \mid \tau) d(x_c, y_c). \tag{2.11}$$

A grid-based approach was used for efficiently evaluating the relevant distributions and estimates. Specifically, the domain $\mathcal{D}$ of interest is discretized using a set of *M* grid points $\{(x_{c,1}, y_{c,1}), (x_{c,2}, y_{c,2}), \ldots, (x_{c,M}, y_{c,M})\} \in \mathcal{D}$. The probability distributions are defined on this set, and respective integrals simplify to summations. Thus, the posterior distribution is now given by

$$\Pr(x_c = x_{c,m}, y_c = y_{c,m} \mid \tau) = \frac{p(\tau \mid x_{c,m}, y_{c,m}) \Pr(x_c = x_{c,m}, y_c = y_{c,m})}{\sum_{m'=1}^{M} p(\tau \mid x_{c,m'}, y_{c,m'}) \Pr(x_c = x_{c,m'}, y_c = y_{c,m'})}, m = 1, 2, \ldots, M, \tag{2.12}$$

and the estimate of the damage location becomes

$$\begin{aligned} (\hat{x}_c, \hat{y}_c)^{mean} &= \sum_{m=1}^{M} (x_{c,m}, y_{c,m}) \Pr(x_c = x_{c,m}, y_c = y_{c,m} \mid \tau), \\ (\hat{x}_c, \hat{y}_c)^{\text{mode}} &= \underset{(x_{c,m}, y_{c,m})}{\arg\max} \Pr(x_c = x_{c,m}, y_c = y_{c,m} \mid \tau). \end{aligned} \tag{2.13}$$

The covariance is

$$\text{Cov}\left[(x_c, y_c) \mid \tau\right] = \sum_{m=1}^{M} \left[(x_{c,m}, y_{c,m}) - (\hat{x}_c, \hat{y}_c)\right]\left[(x_{c,m}, y_{c,m}) - (\hat{x}_c, \hat{y}_c)\right]^T \Pr(x_c = x_{c,m}, y_c = y_{c,m} \mid \tau), \tag{2.14}$$

and

$$p_{\mathcal{D}_s} = \sum_{\left\{m:(x_{c,m}, y_{c,m}) \in \mathcal{D}_s\right\}} \Pr(x_c = x_{c,m}, y_c = y_{c,m} \mid \tau). \tag{2.15}$$

2.1.3. Probabilistic Data Association

The grouped MPD of the received sensor signal contains several wave components with respective time-of-flights. However, it is not known which of these correspond to the reflected A_0 wave from the damage, and which correspond to boundary reflections and other paths unrelated to damage. Since the localization algorithm specifically requires time-of-flight information for the damage-reflected waves, this uncertainty needs to be quantified. The technique of probabilistic data association (PDA) [53, 54] is presented here in order to account for this measurement origin uncertainty within the estimation framework.

Suppose that $\boldsymbol{\tau} = \{\tau_1, \tau_2, \ldots, \tau_L\}$ is a set of L time-of-flight measurements obtained from the grouped MPD of the received sensor signal. The association events A_l, l = 1, 2, . . . , L, are defined such that τ_l is the time-of-flight corresponding to the damage-reflected wave in event A_l. Then, the measurement-uncertainty adjusted likelihood function for the damage location can be written as the mixture

$$p(\boldsymbol{\tau} \mid x_c, y_c) = \sum_{l=1}^{L} p(\tau_l \mid x_c, y_c) \Pr(\mathcal{A}_l \mid \boldsymbol{\tau}), \tag{2.16}$$

where $\Pr(A_l|\boldsymbol{\tau})$ is the probability of the event A_l given the measurements, written as

$$\Pr(\mathcal{A}_l \mid \boldsymbol{\tau}) = \frac{p(\tau_l \mid \mathcal{A}_l)\Pr(\mathcal{A}_l)}{\sum_{l'=1}^{L} p(\tau_{l'} \mid \mathcal{A}_{l'})\Pr(\mathcal{A}_{l'})}, \tag{2.17}$$

with

$$p(\tau_l \mid \mathcal{A}_l) = \int_{\mathcal{D}} p(\tau_l \mid x_c, y_c)\, p(x_c, y_c)\, d(x_c, y_c). \tag{2.18}$$

Here the time-of-flight measurements not corresponding to the damage-reflected wave have been ignored for simplicity and computational efficiency, and $\Pr(A_l)$ is the prior probability of event A_l (taken here as $1/L$). The damage location can be estimated by computing the posterior distribution

$$p(x_c, y_c \mid \boldsymbol{\tau}) \propto p(\boldsymbol{\tau} \mid x_c, y_c)\, p(x_c, y_c), \tag{2.19}$$

and then calculating its mean or mode. For the discretized case, Eqn. (2.18) and Eqn. (2.19) are given by

$$p(\tau_l \mid \mathcal{A}_l) = \sum_{m=1}^{M} p(\tau_l \mid x_{c,m}, y_{c,m}) \Pr\left(x_c = x_{c,m}, y_c = y_{c,m}\right), \tag{2.20}$$

and

$$\Pr\left(x_c = x_{c,m}, y_c = y_{c,m} \mid \boldsymbol{\tau}\right) = \frac{p(\boldsymbol{\tau} \mid x_{c,m}, y_{c,m}) \Pr\left(x_c = x_{c,m}, y_c = y_{c,m}\right)}{\sum_{m'=1}^{M} p(\boldsymbol{\tau} \mid x_{c,m'}, y_{c,m'}) \Pr\left(x_c = x_{c,m'}, y_c = y_{c,m'}\right)}, m = 1, 2, \ldots, M. \quad (2.21)$$

In order to ensure the time-of-flight measurements are accurate, a validation gate is used. If the τ_i corresponding to the maximum value of $\Pr(A_l|\boldsymbol{\tau})$ is within 2σ of the maximum value of $p\left(\tau_l \mid \mathcal{A}_l\right)$, Eqn. (2.19) is used to estimate the damage location. If the τ_i from the maximum value of Eqn. (2.19) falls outside this region, a uniform distribution function over the entire domain is used to describe the posterior distribution. By using this uniform distribution, inaccurate or corrupted time-of-flight measurements do not negatively impact the localization results.

2.1.4. Sensor Fusion

The time-of-flight information obtained from a single transmitter-damage-receiver, or sensor path, is usually insufficient for localizing damage. Data is therefore collected from multiple sensors distributed on the structure, and the time-of-flight information from the various sensor paths is fused to estimate the damage location with higher accuracy. Let $\mathcal{T} = \{\boldsymbol{\tau}_1, \boldsymbol{\tau}_2, \ldots, \boldsymbol{\tau}_N\}$ be a set of time-of-flight measurements obtained from the signals received via N different sensor paths. Here, $\boldsymbol{\tau}_n$ denotes the set of L time-of-flight measurements obtained from the MPD of the received signal for path n. Assuming conditional independence of the time-of-flight measurements from the different sensor paths given the damage location, the fused likelihood function can be expressed as the product of the individual likelihoods:

$$p(\mathcal{T} \mid x_c, y_c) = \prod_{n=1}^{N} p(\boldsymbol{\tau}_n \mid x_c, y_c). \quad (2.22)$$

The posterior probability distribution of the damage location, given the time-of-flight measurements of the various sensor paths, is obtained by combining the likelihood given in Eqn. (2.22) with the prior using Bayes' theorem

$$p(x_c, y_c \mid \mathcal{T}) \propto p(\mathcal{T} \mid x_c, y_c)\, p(x_c, y_c), \tag{2.23}$$

and the sensor-fused estimate $(\hat{x}_c, \hat{y}_c)$ of the damage location is computed as the mean or mode of this posterior:

$$\begin{aligned} (\hat{x}_c, \hat{y}_c)^{mean} &= \int_{\mathcal{D}} (x_c, y_c)\, p(x_c, y_c \mid \mathcal{T}) d(x_c, y_c), \\ (\hat{x}_c, \hat{y}_c)^{\text{mode}} &= \underset{(x_c, y_c) \in \mathcal{D}}{\arg\max}\; p(x_c, y_c \mid \mathcal{T}). \end{aligned} \tag{2.24}$$

Discretization is carried out as before.

2.2. Experimental Algorithm Validation using Fatigued Lug Joint

For algorithm verification and validation, a bulk aluminum 2024-T351 lug joint subjected to fatigue loading was instrumented and interrogated. The dimensions of the lug joint can be seen in Figure 2.6.

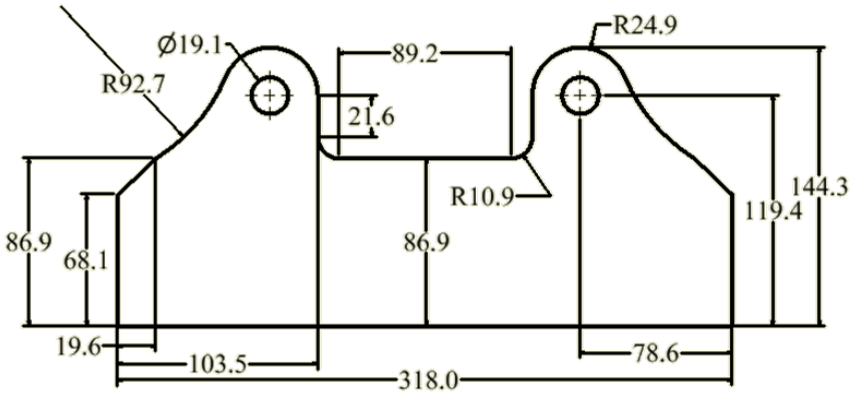

Figure 2.6. Dimensions of aluminum lug joint (dimensions in mm).

The instrumented specimen is shown in Figure 2.7 as well as the servo–hydraulic fatigue frame. The aluminum lug joint, which was machined from bulk Al 2024-T351, was cyclically loaded between 1.3 kN and 13 kN (load ratio of 0.1) at a rate of 5 Hz.

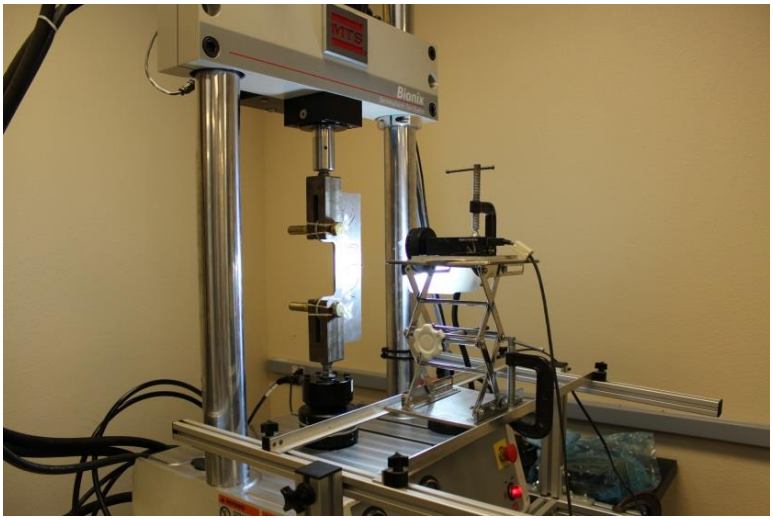

Figure 2.7. Experimental test frame setup used for fatigue loading.

Circular lead zirconium titanate transducers (PZTs) made from APC 851 with a 6.35 mm diameter and 0.25 mm thickness from American Piezo Ltd. were used for sensing and actuation. The PZTs were bonded to the specimen using an off-the-shelf cyanoacrylate adhesive. Seven PZTs were instrumented on the lug joint with a symmetric configuration about the lug joint's plane of symmetry. The locations of the seven PZTs can be seen in Figure 2.8.

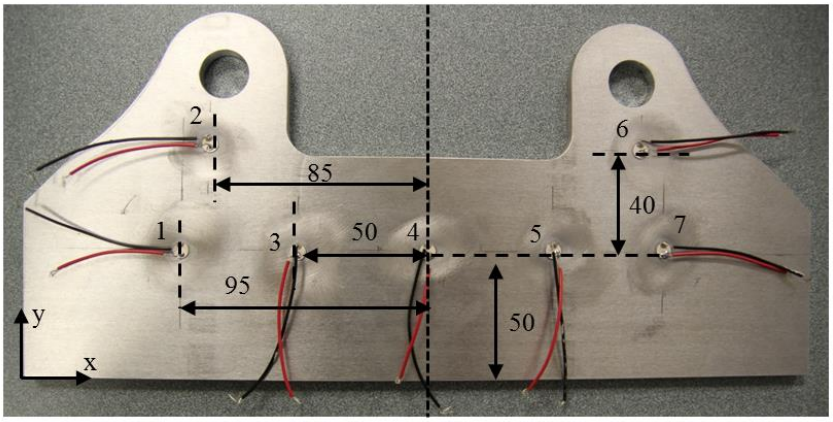

Figure 2.8. Instrumented aluminum lug joint (dimensions in mm).

A National Instruments data acquisition system (model NI PXI 1042) with a 14-bit Arbitrary Waveform Generator (AWG, model NI PXI-5412), and a 12-bit high-speed digitizer (DIG, model NI PXI-5105) was utilized to interrogate the specimen. A windowed cosine signal with a 500 kHz central frequency was used as the actuation signal. A round-robin interrogation approach was used to collect data from each sensor path. The response along each sensor path was measured ten times and averaged in order to increase the signal to noise ratio.

2.2.1. Wave Velocity Model Verification

Before the damage localization algorithm can be used, the model assumed for the wave velocity in (2.5) must be verified. The velocity model used assumed a Gaussian distribution for the time-of-flights, with the mean at the theoretical time-of-flight assuming isotropic wave propagation from the actuator to the damage, to the sensor, and the variance corresponding to the measurement uncertainty for the sensor path. To verify this assumption, a healthy lug joint at room temperature was interrogated 100 times along each sensor path and the time-of-flight distribution was observed.

The time-of-flights corresponding to the direct A_0 wave for the 1-4 and 4-7 sensor paths actuated at 500 kHz can be seen in Figure 2.9.

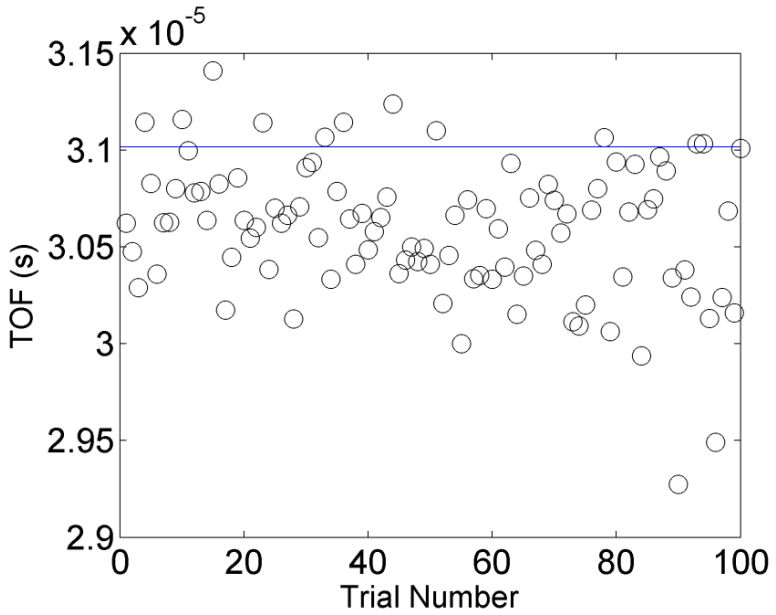

Figure 2.9. Sensor path 1-4 and 4-7 time-of-flight distribution data.

The solid line in Figure 2.9 represents the theoretical time-of-flight for the 500 kHz A_0 mode, while the markers represent the experimental time-of-flights. Clearly, there is a significant time shift between the theoretical and experimental time-of-flights. The velocity model in (2.5) assumes a distribution about the theoretical time so the time shift seen in the experimental data must be accounted for by using

$$\tau = \overline{t}_{\text{exp}} + \delta \tag{2.25}$$

where τ is the time-of-flight in (2.5), $\overline{t}_{\text{exp}}$ is the mean of the experimental time-of-flight distribution, and δ is the mean time shift. Using (2.25), the time-of-flight distribution becomes distributed about the theoretical time as required in the assumed model.

The next step to validate the velocity model is to ensure the time-of-flight distribution is Gaussian. The experimental time-of-flight distribution for the A_0 mode actuated at 500 kHz along the 1-4 or 4-7 sensor paths is shown in Figure 2.10.

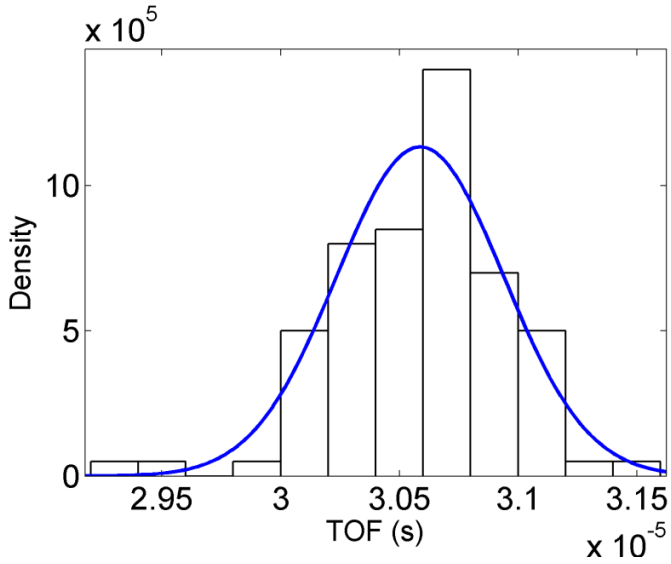

Figure 2.10. Sensor path 1-4 and 4-7 time-of-flight distribution.

Figure 2.10 shows that the 500 kHz A_0 mode follows the Gaussian distribution very closely, seen here in blue. A chi-square test was conducted on the experimental data to confirm that the distribution was Gaussian. The standard deviation for the sensor path was chosen by averaging the difference between the maximum value and the mean value of the distribution, with the difference between the mean value and the minimum value of the distribution. The mean shifts and standard deviations used in this investigation for each sensor path can be seen in Table 2.1.

Table 2.1. Sensor path mean shift and standard deviation.

Sensor Path	**Mean Shift, δ (μs)**	**Standard Deviation, σ (μs)**
2-5, 3-6	-0.8	4.0
1-5, 3-7	-1.9	3.0
2-4, 4-6	-1.6	4.4
1-4, 4-7	0.4	1.1

Table 2.1 shows that the standard deviation in the time-of-flight measurements is a strong function of the sensor path. The sensor arrangement used in this investigation is a modified version of that found in [7], where the placement was optimized based upon sensing radius. In [7] only three sensors were required to localize damage on either shoulder because mode converted waves were used in the localization. The arrangement was modified by adding sensors 3 and 5 because more sensors are required when using only the A_0 mode to localize damage. The results in Table 2.1 show that for damage localization, sensor placement should be optimized to decrease the variance in their measurements. This could be accomplished by optimizing sensor placement to localize damage growing in a certain location, and ensuring the time-of-flights received from the damage are significantly different from those received from boundary reflections.

2.2.2. Damage Localization Results

The aluminum lug joint, which was machined from bulk Al 2024-T351, was cyclically loaded between 1.3 kN and 13 kN (load ratio of 0.1) at a rate of 5 Hz. After crack initiation, the loading frequency was reduced in order to more easily interrogate the structure at multiple crack lengths. To track the crack growth, a camera with a macro lens was mounted in front of the specimen and was focused in one of two hot spots (top and bottom shoulders); another camera was placed behind the fatigue frame and focused on both hot spots. Images were captured along with the sensor data. The images were used to compute the crack length through digital measurements. The locations of the crack tip are listed in Table 2.2 and use the coordinate system defined in Figure 2.8.

Table 2.2. Experimental (x,y) crack tip location and length versus number of fatigue cycles.

Cycles	(x,y) Crack Tip Location (mm)	Crack Length (mm)
81,761	(207.4, 86.4)	1.6
85,537	(207.7, 85.3)	2.8
86,106	(208.2, 84.6)	3.7
86,248	(209.0, 83.3)	5.2
86,889	(210.0, 82.3)	6.6
87,737	(210.6, 81.3)	7.8
88,208	(211.7, 80.6)	9.0
88,819	(212.4, 78.7)	11.1
89,247	(213.0, 77.4)	12.5
89,557	(213.8, 75.8)	14.3
89,794	(214.2, 74.2)	16.0
90,076	(214.4, 72.3)	17.9
90,417	(215.1, 69.7)	20.6

The signals from the experimental fatigue of a lug joint were used to validate the localization algorithm. At each cycle where the fatigue crack length was measured, data from the PZTs was collected and the localization algorithm was applied. The sensor paths used to localize the damage are sensor paths 3-6, 3-7, 4-6, and 4-7 due to the fatigue crack growing on the right shoulder of the lug joint. From finite element simulations and previous work on lug joints [7], it is shown that the hot spots for fatigue crack growth are the shoulders of the lug joint. Therefore, a truncated multivariate Gaussian prior probability was applied to the lug joint near the shoulder, with a mean location of (211, 80) mm and the covariance parameters shown in Table 2.3.

Table 2.3. Covariance matrix parameters.

Covariance Parameters	Value (mm)
σ_{xx}	15.0
σ_{xy}	0.0
σ_{yx}	0.0
σ_{yy}	15.0

The prior probability distribution was chosen to cover the entire region the crack was expected to grow in with high probability. The resulting prior distribution over the lug joint domain can be seen in Figure 2.11.

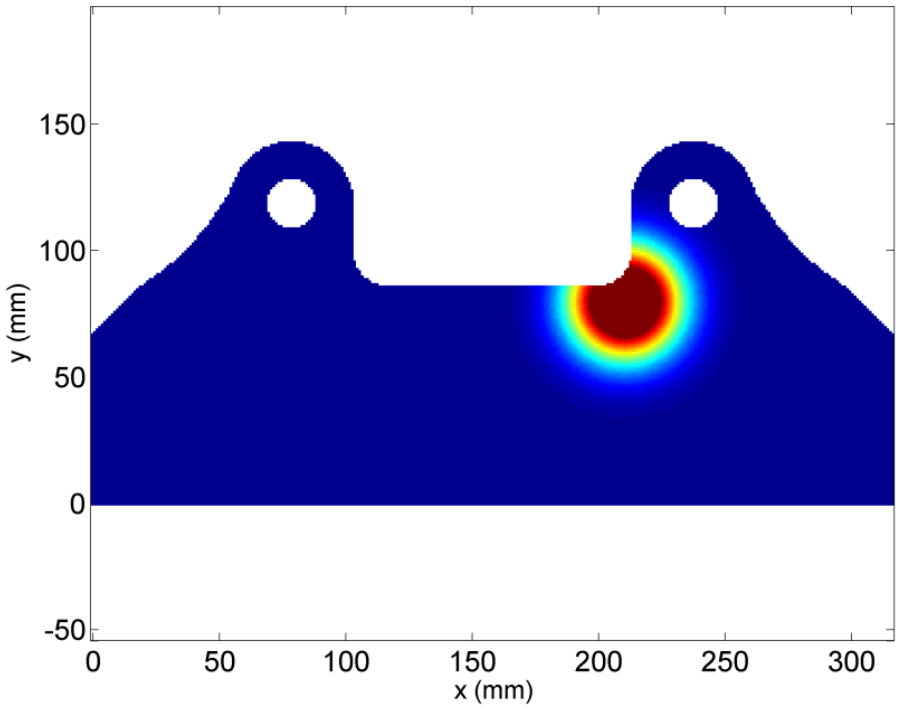

Figure 2.11. Lug joint prior knowledge.

The result for the probabilistic damage localization at 86,106 cycles can be seen in Figure 2.12.

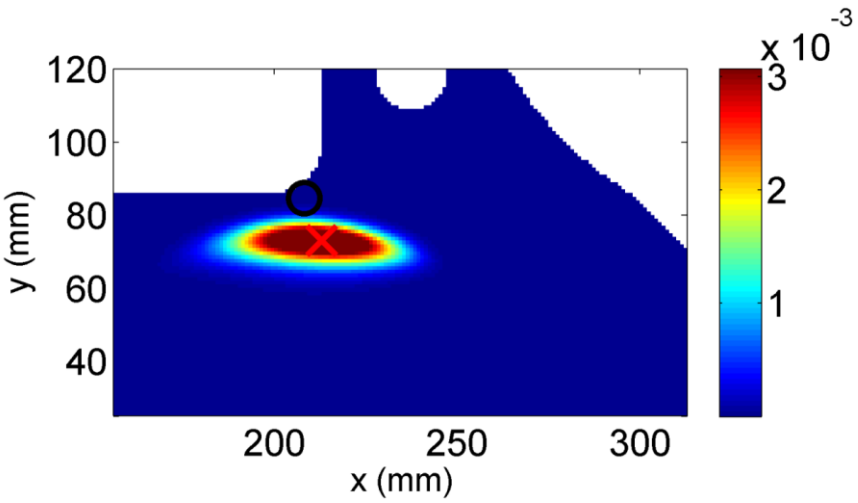

Figure 2.12. Damage localization for cycle 86,106 with o denoting true damage location and x as estimated damage location.

In Figure 2.12, the black circle represents the true damage location while the red cross represents the estimated damage location using the maximum probability location. The damage localized in Figure 2.12 corresponds to a 3.7 mm surface crack. With the damage so close to the boundary there is a large error in the localization. This error is due to the small difference between the time-of-flight from damage near the boundary, and that from the boundary. The small time-of-flight difference coupled with the measurement errors cause error whenever damage is localized near a boundary.

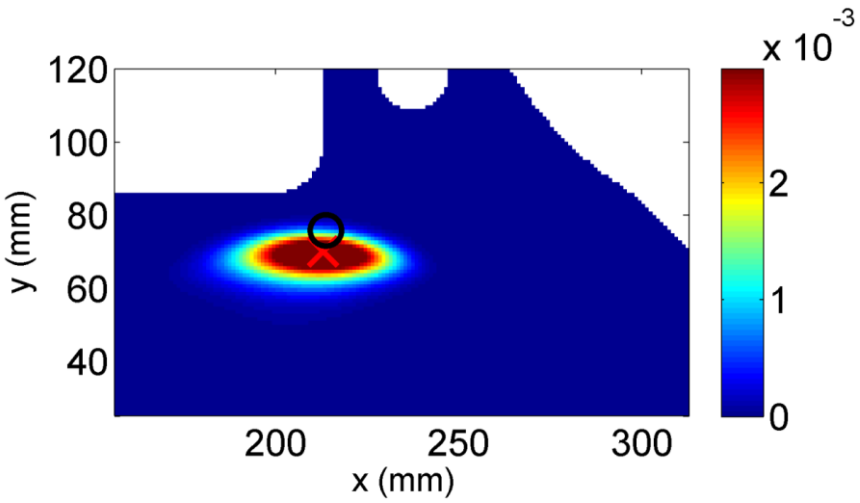

Figure 2.13. Damage localization for cycle 89,557 with o denoting true damage location and x as estimated damage location.

The damage localization result for 89,557 cycles can be seen in Figure 2.13, which shows that as the damage moves away from the boundary, the localization error decreases. With the true damage location being farther from the boundary the localization algorithm is able to place a region of high probability near the true location. This region of high probability is sufficiently small, such that if the lug joint was taken out of service for a visual inspection the damage could be quickly discovered using the results of the localization algorithm.

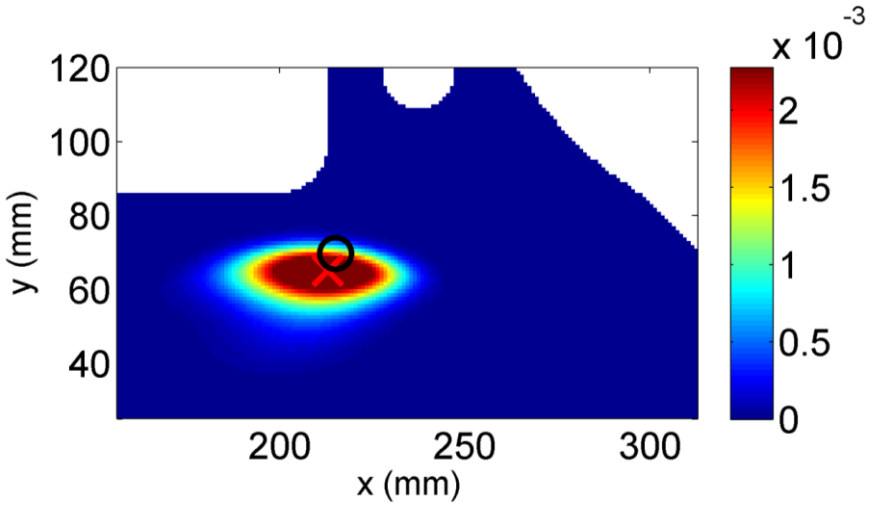

Figure 2.14. Damage localization for cycle 90,417 with o denoting true damage location and x as estimated damage location.

The damage localization results for 90,417 cycles can be seen in Figure 2.14. The same trend of improved localization performance as the damage moves farther away from the boundary of the lug joint is also observed from this figure. The localization error, or distance between the true damage location and the estimated damage location, can be seen in Table 2.4.

Table 2.4. Localization error in lug joint fatigue test.

Cycles	**(x,y) (mm)**	**Error (mm)**
81,761	(212,87)	4.64
85,537	(216,67)	20.11
86,106	(213,73)	12.52
86,248	(209,83)	0.31
86,889	(208,82)	2.01
87,737	(212,71)	10.37
88,208	(207,86)	7.16
88,819	(216,67)	12.23
89,247	(210,77)	3.00
89,557	(213,70)	5.83
89,794	(212,76)	2.87
90,076	(216,65)	7.47
90,417	(213,65)	5.15

Table 2.4 confirms the trend of decreasing localization error as the fatigue crack grows in length. The average localization error using the proposed algorithm was found to be 7.21 mm. While the localization error for the proposed algorithm is somewhat large, it is a byproduct of the probabilistic data association framework. The data association framework incorporates every time-of-flight from the grouped MPD feature extraction. By incorporating every time-of-flight with data association weighting, the estimation will never be completely correct but will also never be completely wrong, proving that it is more robust than traditional techniques. Additionally, using data association allows the algorithm to account for the measurement uncertainty and function without any user input, and operate in an unsupervised manner.

2.3. Concluding Remarks

This chapter has shown the difficulties of localizing damage in complex-geometry metallic structures. Specifically, accurate quantification of the uncertainty in a localization system has been shown to be necessary for accurate localization results. The experimental study has shown that probabilistic data association is a capable framework for uncertainty quantification in an SHM localization system. While the localization error is slightly higher using data association than with other methods, the algorithm was able to place a region of high probability around the damaged region without the use of baseline signals. The greatest strength of the data association framework is that the approach can effectively account for the uncertainty, and combine all of the time-of-flights a feature extraction algorithm provides without any additional input from the user.

This study has also shown that the localization error is directly related to the variance in the time-of-flight measurements in each sensor path. The sensor paths used in

this investigation had a range in standard deviation from approximately 1 μs to 4.5 μs. If the variance in the measurements could be decreased, the result would be a more accurate and more concentrated localization of damage. Based on these findings, sensor placement should be optimized to produce a minimum variance in the time-of-flight measurements in order to generate better localization results.

While the probabilistic localization framework presented in this chapter was applied to an aluminum lug joint, the framework can be applied to many different materials and geometries. With further research the localization framework could be extended to anisotropic materials by modifying the assumed isotropic velocity propagation model. Also, the framework can easily be modified to include a physics-based damage evolution model. By incorporating a damage evolution model the prior distribution could be updated dynamically to the predicted crack tip location, and result in more accurate localizations with a smaller variance. Finally, the framework also has the ability to be extended in order to become a detection algorithm. If a numerical model were able to accurately describe the path every wave travels from actuator to sensor, the information could be used along with the association events to determine if the measured time-of-flights corresponds to an undamaged structure.

Chapter 3

PROBABILISTIC DAMAGE LOCALIZATION AT UNKNOWN TEMPERATURES

Damage localization at unknown temperatures is one of the primary challenges that guided wave SHM systems face. Temperature affects every component of an SHM localization system, from the characteristics of the sensors to the structural response of the material being interrogated. In order to develop a robust localization framework that can function at any temperature, the framework must become independent of any parameters that can be influenced by temperature. This chapter presents an approach to estimate a structure's temperature and wave speeds using *in situ* signals, and then to incorporate the estimated wave speed in to the probabilistic localization algorithm. The proposed algorithm was applied to a complex-geometry metallic structure with growing fatigue damage at a range of temperatures. The objective was to demonstrate the ability of the algorithm to accurately estimate the temperature and wave speed in a structure, and use the estimated values to improve damage localization performance. Section 3.1 describes the method used to estimate temperature and wave speed. Section 3.2 presents the updated probabilistic damage localization algorithm using the temperature and velocity estimation algorithm. Section 3.3 and Section 3.4 describe the experimental and numerical techniques used to validate the performance of the proposed algorithm. Finally, Section 3.5 provides concluding remarks on the algorithm and the results.

3.1. Creating a Velocity-Temperature Model

When attempting to localize damage at an unknown temperature the largest factor contributing to error is uncertainty in the speed of the wave that is interrogating the damage [46]. In a typical localization scheme, a fixed wave speed is chosen that would be

representative of the wave speed in the structure. In reality, however, structural components will often be interrogated at unknown temperatures; therefore, the true wave speed will often not be known. The proposed approach estimates the velocity of the wave actually present in the structure, and utilizes this velocity in the localization algorithm.

The first step in localizing damage at an unknown temperature is to obtain a model of how the group velocity changes with temperature. The model was selected to represent temperatures from -60°C to 160°C. This temperature range was chosen because it represents a maximum temperature range in which a guided wave system using PZTs could be expected to operate. Material properties used in the model were found in approximately 10°C increments from MIL-HDBK-5 [60]. To gain a finer temperature resolution a linear interpolation function was used inside the 10°C region to determine the velocity in 1°C increments. The material used in this work is aluminum 2024-T351 with a room temperature Young's Modulus, E, of 73.77 GPa and a Poisson's ratio, ν, of 0.33. MIL-HDBK-5 also provides information on the effect of temperature on E. E was found to vary from 105% of the room temperature value at -60°C, to 94% of the room temperature value at 160°C. Using these material properties, the theoretical dispersion curves for aluminum 2024-T351 were computed in the temperature range of -60°C to 160°C and can be seen in Figure 3.1.

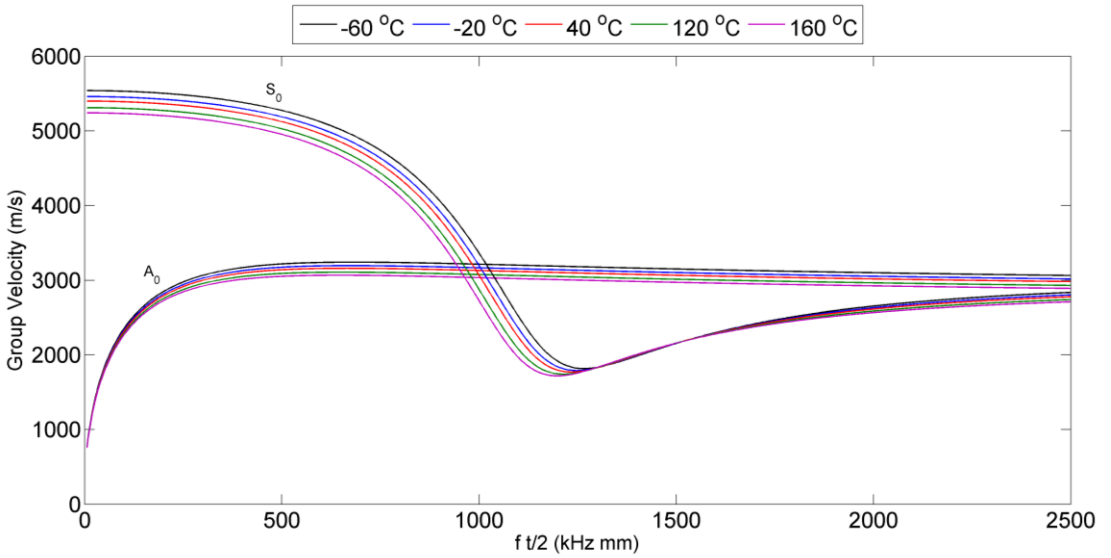

Figure 3.1. Theoretical dispersion curves for Al 2024-T351 at various temperatures.

The theoretical dispersion curves in Figure 3.1 show that the velocity of the waves decreases with an increase in temperature, as expected, because the stiffness of the material decreases.

Next, in order to estimate the velocity, a parameter must be chosen that is sensitive to temperature and can be related back to the localization velocity. For this material, the S_0 mode actuated at 250 kHz was found to be very sensitive to temperature, as is shown in Figure 3.2, and was chosen as the parameter to estimate the 500 kHz A_0 localization velocity. To select this frequency, the frequency-thickness in Figure 3.1 that had the largest range of velocities for the temperatures investigated was chosen. The frequencies used for temperature estimation and localization can be different if the localization frequency is not found to be sensitive to temperature.

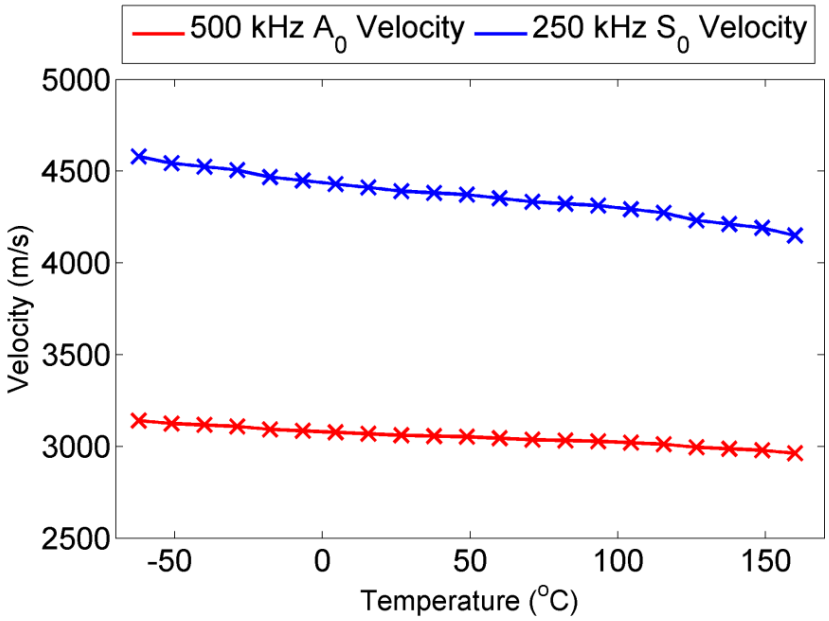

Figure 3.2. Group velocity-temperature relationship for 250 and 500 kHz Lamb waves.

The markers in Figure 3.2 represent the temperatures at which material properties were available, while the lines represent the velocity-temperature model using the linear interpolation function. In order to save on computational time during damage localization the corresponding velocities and temperatures are stored in an offline velocity-temperature dictionary. Also seen in Figure 3.2; for an actuation frequency of 250 kHz the S_0 mode would be the first arriving mode at a sensor and therefore easy to detect.

3.1.1. Methods to Estimate Temperature and Localization Velocity

With the actuation frequency for velocity estimation chosen, and with a model for the effect of temperature on wave speeds found, the temperature and velocity estimation algorithm can now be completely defined. First, the sensor-actuator pairs that will be used for velocity estimation are actuated at 250 kHz. Each recorded signal is then passed into the grouped MPD algorithm defined in Section 2.1.1. The first time-of-flight from the grouped

MPD algorithm for each signal is then extracted because the S_0 mode is the first arriving mode at 250 kHz, as seen from Figure 3.2. Each time-of-flight is then converted to a velocity using the known distance between the sensors and actuators. These calculated velocities for the 250 kHz S_0 mode are then mapped to a set of temperatures by finding the temperatures that correspond to a minimum difference between the calculated velocities and the velocities in the velocity-temperature dictionary. The temperature of the structure can be estimated by averaging the set of temperatures found using this dictionary. Once the set of temperatures is found, a corresponding set of A_0 velocities at 500 kHz can be obtained using the dictionary. Time-of-flights of the 500 kHz A_0 modes are then calculated through dividing the distances between the actuators and receivers by their respective estimated velocities.

With the expected time-of-flights, the 500 kHz A_0 velocity can be estimated in one of three ways assuming a Gaussian distribution and a known variance in the time-of-flight measurements. The first velocity estimate can be computed using the maximum likelihood (ML) method. For the ML case, the estimated velocity, v^*, can be found using

$$v_{ML}^{*} = \arg\max_{(v)} \ln\left(\prod_{i=1}^{N} \frac{1}{\sqrt{2\pi}\sigma} e^{-\left(\tau_i - d_i/v\right)^2 / 2\sigma^2} \right) \tag{3.1}$$

where N is the number of sensor paths, d_i is the distance between sensor and actuator for sensor path i, τ_i is the time-of-flight for sensor path i, σ is the standard deviation in the time-of-flight measurements, and v is velocity. For the Gaussian setting, the expression for the estimated velocity using the ML method can be simplified to

$$v_{ML}^{*} = \frac{\sum_{i=1}^{N} d_i^2}{\sum_{i=1}^{N} \tau_i d_i}. \tag{3.2}$$

A second estimator of the velocity can be found using the minimum mean square error (MMSE) method. This method finds the velocity probability density function (PDF) for each sensor path, optimally combines each of the PDFs, and finally finds the mean of the optimally-combined PDF using

$$v_{MMSE}^{*} = \frac{\int v \cdot \prod_{i=1}^{N} \left(\frac{1}{\sqrt{2\pi}\sigma} e^{-\left(\tau_i - d_i/v\right)^2 / 2\sigma^2} \right) dv}{\int \prod_{i=1}^{N} \left(\frac{1}{\sqrt{2\pi}\sigma} e^{-\left(\tau_i - d_i/v\right)^2 / 2\sigma^2} \right) dv}. \tag{3.3}$$

The mean velocity of the velocity PDF is found by using the measured time-of-flight τ_i, distance d_i, and standard deviation σ, from each of the N sensor paths. In both the ML and MMSE methods, the estimated velocity v^* is directly entered as an input into the localization algorithm, and no other information about the velocity PDF is used.

The final method investigated to estimate the velocity is the full integration method. Unlike the ML and MMSE methods, the full integration method uses the entire optimally-combined velocity PDF which is defined as

$$p(v) \propto \prod_{i=1}^{N} \left(\frac{1}{\sqrt{2\pi}\sigma} e^{-\left(\tau_i - d_i/v\right)^2 / 2\sigma^2} \right). \tag{3.4}$$

Every velocity in the optimally-combined velocity PDF is then used to localize the damage. The final localization result is the sum of every localization, weighted by the probability of that velocity as

$$p(x_c, y_c) = \int p(x_c, y_c \mid \tau(V))\, p(V)\, dV. \tag{3.5}$$

In this investigation, the ML method is the only method used and discussed in the future sections. The ML method was selected because it provided the most accurate results with the least computational time.

3.2. Probabilistic Damage Localization Algorithm with Temperature and Velocity Estimation

To summarize, the proposed algorithm, shown in Figure 3.3, can be separated into two main stages: temperature estimation and damage location estimation. The first step of the temperature estimation stage is to actuate and sense a 250 kHz signal for every sensor pair used to estimate the velocity. Second, the S_0 wave speed at 250 kHz and the temperature are estimated from the signal. Third, the estimated temperature is mapped to a velocity for the 500 kHz A_0 mode. Fourth, the 500 kHz estimated A_0 velocities found from each sensor path are optimally combined and given to the localization algorithm.

The first step for the damage location estimation stage is to discretize the domain being interrogated. Second, the structure is interrogated using a 500 kHz actuation signal and the signals in each sensor path are subtracted. Third, the differenced signal is decomposed using the grouped MPD algorithm for each sensor path. Fourth, the time-of-flights extracted from the MPD algorithm are submitted into the Bayesian probabilistic localization algorithm. Fifth, the validation gate is used to ensure time-of-flight

measurement accuracy. Sixth, the localization results from each sensor path are fused to create the final probabilistic damage localization result.

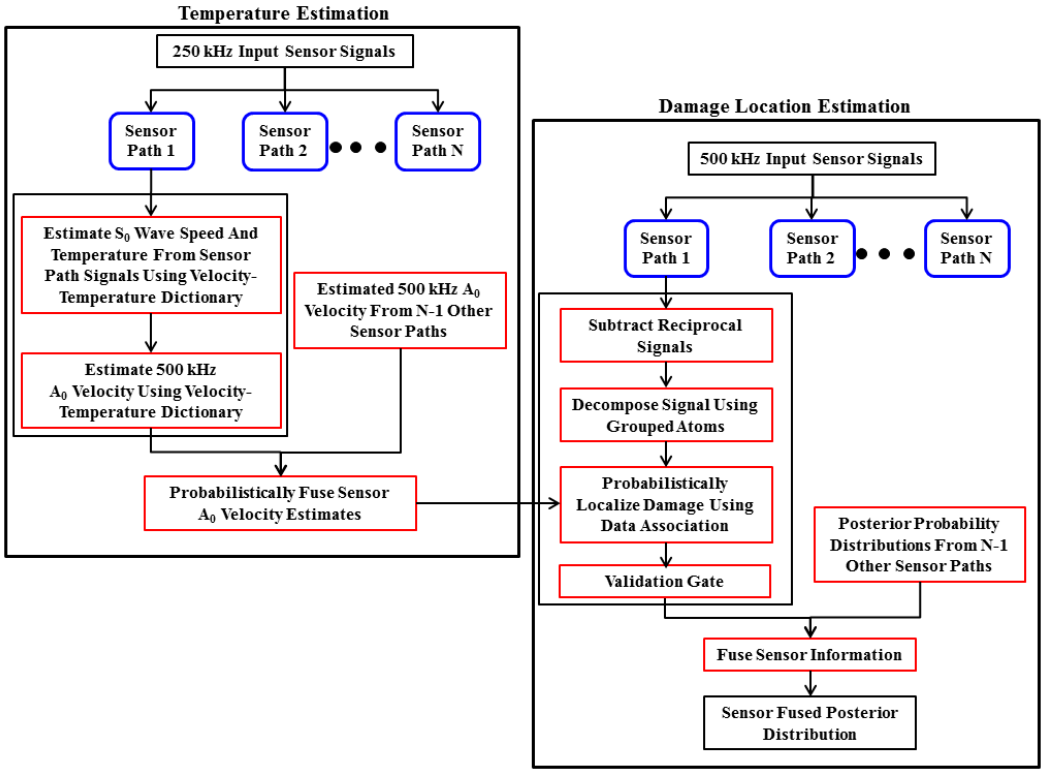

Figure 3.3. Flow chart of probabilistic localization algorithm with temperature and velocity estimation.

3.3. Experimental Algorithm Validation using Fatigued Lug Joint

The same lug joint experimental data presented in Section 2.2 for known temperature damage localization is used to validate the damage localization algorithm using temperature and velocity estimation. The sensor paths used to localize the damage are sensor paths 3-6, 3-7, 4-6, and 4-7 while the temperature and velocity estimation algorithm uses sensor path 1-7. Sensor path 1-7 was chosen for temperature and velocity estimation because it is the longest direct sensor path which means the waves along this path will be the most widely separated in time reducing the measurement error.

In order to localize damage on the lug joint over a range of temperatures, a Cascade-Tek forced air lab oven was used. At 13 different fatigue cycles the lug joint was removed from the fatigue frame, placed in the oven, and interrogated using the PZTs at temperatures of 20°C, 40°C, 60°C, and 80°C. After the lug joint was interrogated it was cooled to room temperature, reinstalled on the fatigue frame, and the test was continued. Higher temperatures were not investigated experimentally because the bonding adhesive and the PZT wiring used were not capable of operating at higher temperatures.

The damage localization using temperature and velocity estimation algorithm was verified in three tests. The first test ensured that the 250 kHz S_0 wave followed the wave velocity model presented in Section 2.1.2. The second test was used to show that the algorithm could accurately predict temperature and wave velocity using only the collected sensor signals. The third test showed the benefits of using a temperature and velocity estimation algorithm when localizing damage at unknown temperatures.

3.3.1. Wave Velocity Model Verification

The temperature and velocity estimation algorithm uses the 250 kHz S_0 mode, so the wave velocity model in (2.5) must be once again verified. The time-of-flights corresponding to the direct S_0 wave for the 1-7 sensor path actuated at 250 kHz can be seen in Figure 3.4.

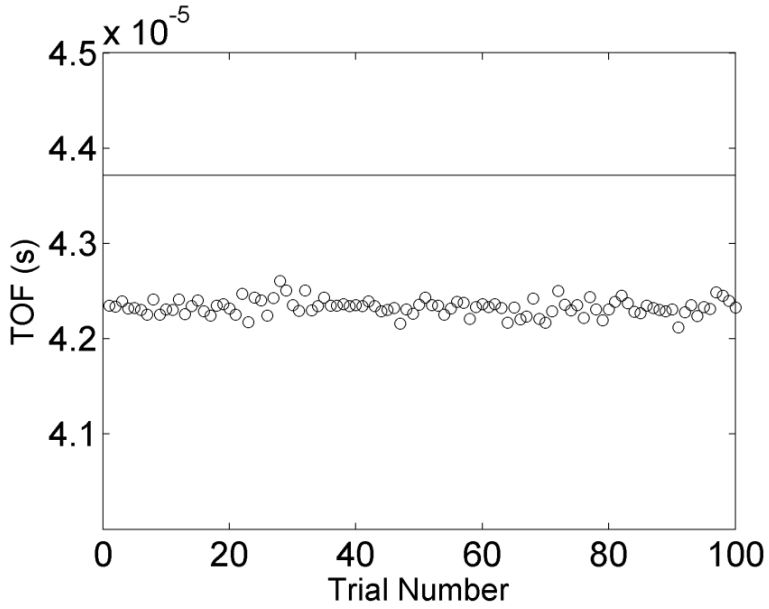

Figure 3.4. Sensor path 1-7 time-of-flight data.

The solid line in Figure 3.4 represents the theoretical time-of-flight for the 250 kHz S_0 mode, while the markers represent the experimental time-of-flights. A significant time shift between the theoretical and experimental time-of-flights is seen in Figure 3.4, similar to what was seen with the 500 kHz A_0 mode. The experimental mean time-of-flight is shifted to the theoretical value using (2.25) in order for the assumed model to be valid. The mean shift for the 1-7 sensor path was found to be 1.2 μs.

The next step to validate the velocity model for velocity and temperature estimation is to ensure the time-of-flight distribution is Gaussian. The experimental time-of-flight distribution for the S_0 mode actuated at 250 kHz along the 1-7 sensor path is shown in Figure 3.5.

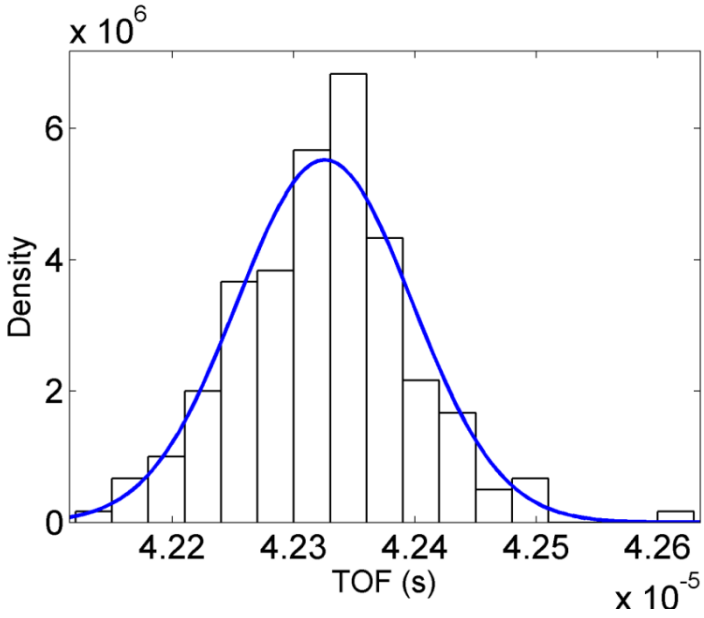

Figure 3.5. Sensor path 1-7 time-of-flight distribution.

Figure 3.5 shows that like the 500 kHz A_0 mode, the 250 kHz S_0 mode also follows the Gaussian distribution, shown in blue. To confirm the distribution was Gaussian, a chi-square test was conducted on the experimental data. The standard deviation for the 1-7 sensor path was defined in the same way as the fixed velocity case and was found to be 0.2 μs.

3.3.2. Temperature Estimation Results

The ability of the proposed algorithm to estimate temperature was validated using the undamaged lug joint and a Cascade-Tek forced air lab oven. For this validation the lug joint was tested at 20°C, 30°C, 40°C, 50°C, 60°C, 70°C, and 80°C. Temperatures above and below this range were not tested due to limitations with the sensor wiring and adhesives. The temperatures investigated were significantly less than the recommended maximum sensor temperature, which is half of the Curie point (360°C) [61]. In this test, the

sensor paths used for velocity estimation were actuated for 20 trials at each testing temperature.

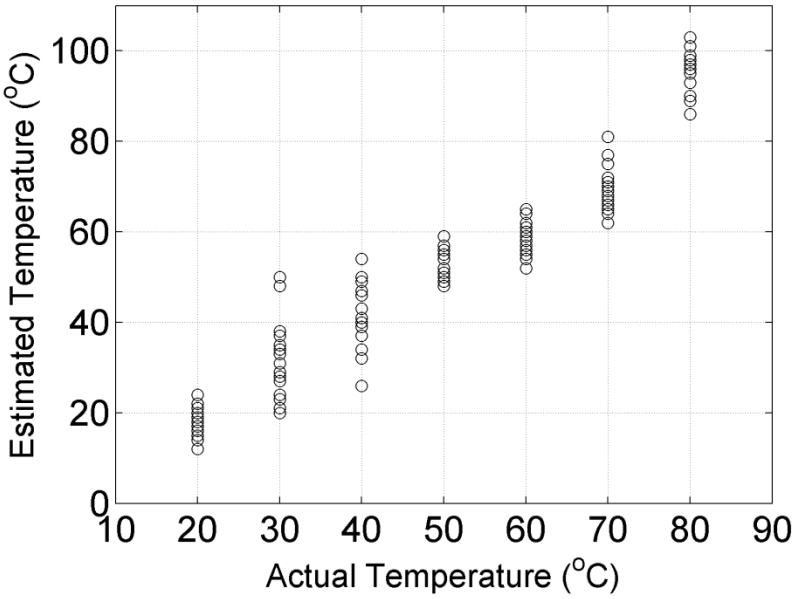

Figure 3.6. Actual and estimated experimental lug joint temperatures.

Figure 3.6 shows that this algorithm can accurately predict temperature variations. The mean temperature of the experimental distributions at temperatures less than 70°C was found to be less than 4°C from the actual temperature. The error was found to increase at 80°C to nearly a 15°C difference, corresponding to a velocity difference of approximately 12 m/s. This increase in error may be attributed to temperature effects on the sensors, adhesives, and DAQ system. This strong correlation between the actual and estimated temperatures for the temperature range tested shows that the mean shift incorporated using Eqn. (2.25) is not a function of temperature.

3.3.3. Fatigued Lug Joint Experimental Results

The algorithm has previously shown that it can accurately estimate temperature when the lug joint is healthy; however, it must also be shown that the presence of damage will not affect the ability of the algorithm to estimate temperature. The estimated temperature and the corresponding fatigue cycle number can be seen in Table 3.1.

Table 3.1. Fatigued lug joint estimated temperatures.

	Estimated Temperature			
Cycles	**20°C**	**40°C**	**60°C**	**80°C**
81,761	12	41.5	57	88.5
85,537	24	45.5	61.5	88
86,106	16	32	59.5	82
86,248	17	33.5	59.5	84.5
86,889	23.5	44.5	59	67.5
87,737	19.5	43	65	69
88,208	21.5	50.5	64.5	48
88,819	34.5	54.5	66.5	49.5
89,247	20	52	69	52.5
89,557	29.5	48	66.5	49.5
89,794	26.5	46.5	67	39
90,076	18.5	37.5	16.5	40
90,417	14.5	31.5	55	55

Table 3.1 shows that the algorithm accurately estimates the temperature of the lug joint even as the fatigue crack grows. The average temperature estimation error is 1.3°C, 3.1°C, 1.0°C, and 17.5°C for 20°C, 40°C, 60°C, and 80°C respectively. Similar to the results seen in Section 3.3.2, the temperature estimation error is very small in the 20°C, 40°C, and 60°C cases but grows significantly at 80°C. This increase in error may be attributed to temperature effects on the sensors, adhesives, and DAQ system.

Using the results from the temperature estimation, the velocity estimation error can be characterized and can be seen in Table 3.2.

Table 3.2. Percent difference between estimated and theoretical velocity.

	Velocity Percent Difference			
Cycles	**20°C**	**40°C**	**60°C**	**80°C**
81,761	0.212	-0.012	0.095	-0.096
85,537	-0.063	-0.030	-0.014	-0.090
86,106	0.116	0.132	0.035	-0.017
86,248	0.105	0.114	0.035	-0.047
86,889	-0.051	-0.018	0.047	0.273
87,737	0.045	-0.006	-0.098	0.274
88,208	-0.003	-0.126	-0.086	0.659
88,819	-0.224	-0.205	-0.135	0.635
89,247	0.033	-0.144	-0.195	0.568
89,557	-0.164	-0.084	-0.135	0.622
89,794	-0.105	-0.042	-0.147	0.774
90,076	0.069	0.066	0.807	0.762
90,417	-0.051	-0.096	-0.062	0.592

Table 3.2 shows that the proposed algorithm is capable of estimating velocity even while a damage is growing. From Table 3.2, the largest velocity estimation error was found to be 0.807%, which corresponds to a velocity difference of 25 m/s. These results further validate the ability of the estimation algorithm to predict and adapt to unknown temperature changes.

With the temperature and velocity estimation portion of the algorithm verified, the localization algorithm performance must now be tested. The localization results from the PZT signals at 20°C, 40°C, 60°C, and 80°C for 86,106 cycles are shown in Figure 3.7.

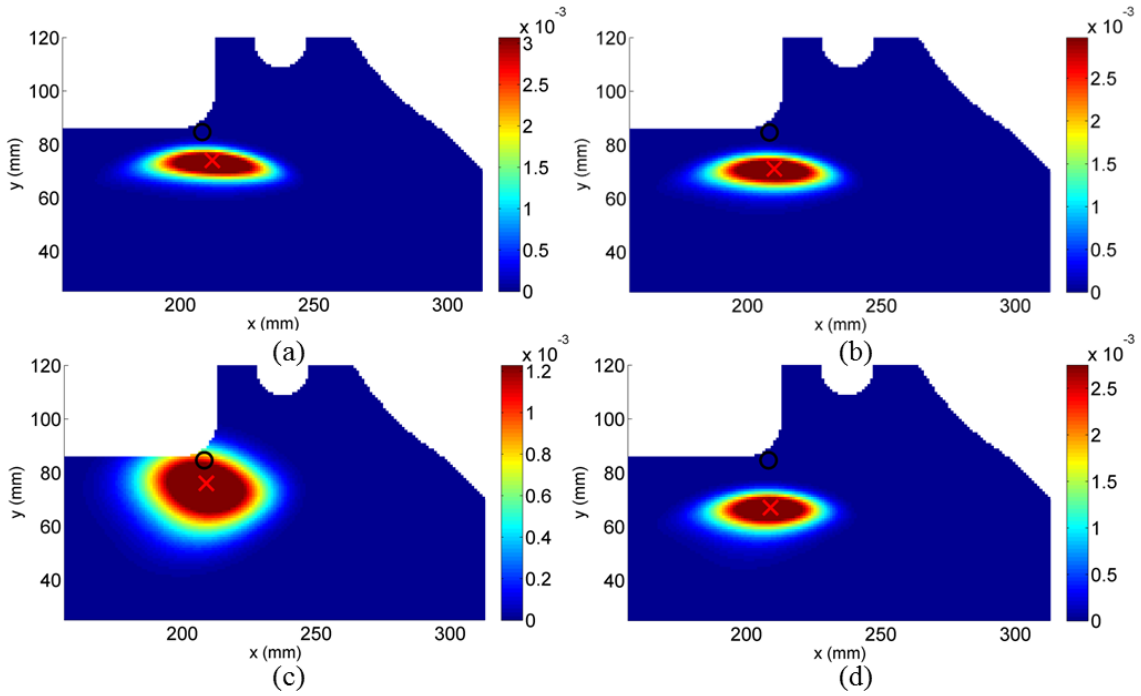

Figure 3.7. 20°C (a), 40°C (b), 60°C (c), and 80°C (d) localizations for cycle 86,106 with o denoting true damage location and x as estimated damage location.

The damage shown in Figure 3.7 corresponds to a 3.7 mm surface crack. The results show that, clearly, the localization algorithm cannot localize a crack of this size and at this location, because the true position lies far outside the region of high probability. The reason that the true location is outside the region of high probability is that time-of-flight estimations have an error associated with the sensor measurements, and that error directly relates to the distance damage must be from a boundary in order for the damage to be accurately localized. Therefore, damage near a boundary, or in a location which would give a time-of-flight estimate similar to that of one from a boundary, is difficult to localize. In order to overcome this limitation, either the measurement errors must be decreased, the feature extraction algorithms improved, or the sensor placement optimized to obtain time-of-flights from damage at significantly different times than those from the boundaries.

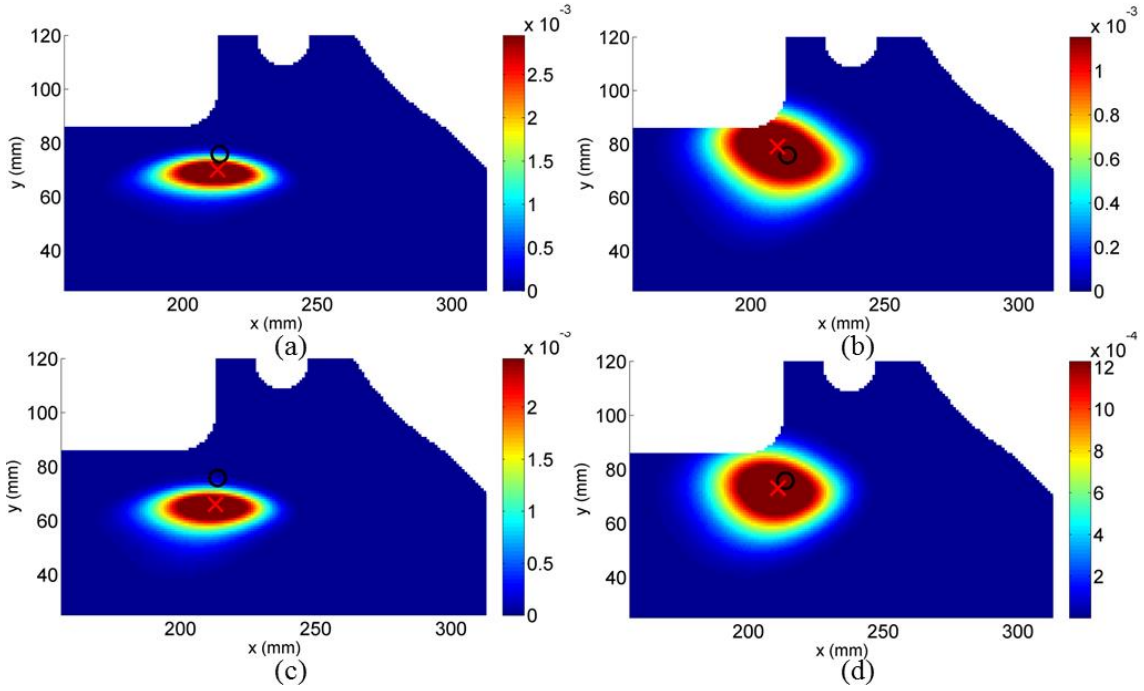

Figure 3.8. 20°C (a), 40°C (b), 60°C (c), and 80°C (d) localizations for cycle 89,557 with o denoting true damage location and x as estimated damage location.

The localization results for the 14.3 mm crack found at 89,557 cycles are shown in Figure 3.8. This figure shows the increase in accuracy of the localization algorithm as the crack tip location moves farther away from the boundary of the lug joint. For this case, the localization error was found to be 5.83 mm, 4.96 mm, 9.80 mm, and 3.92 mm for the four temperatures shown in Figure 3.8.

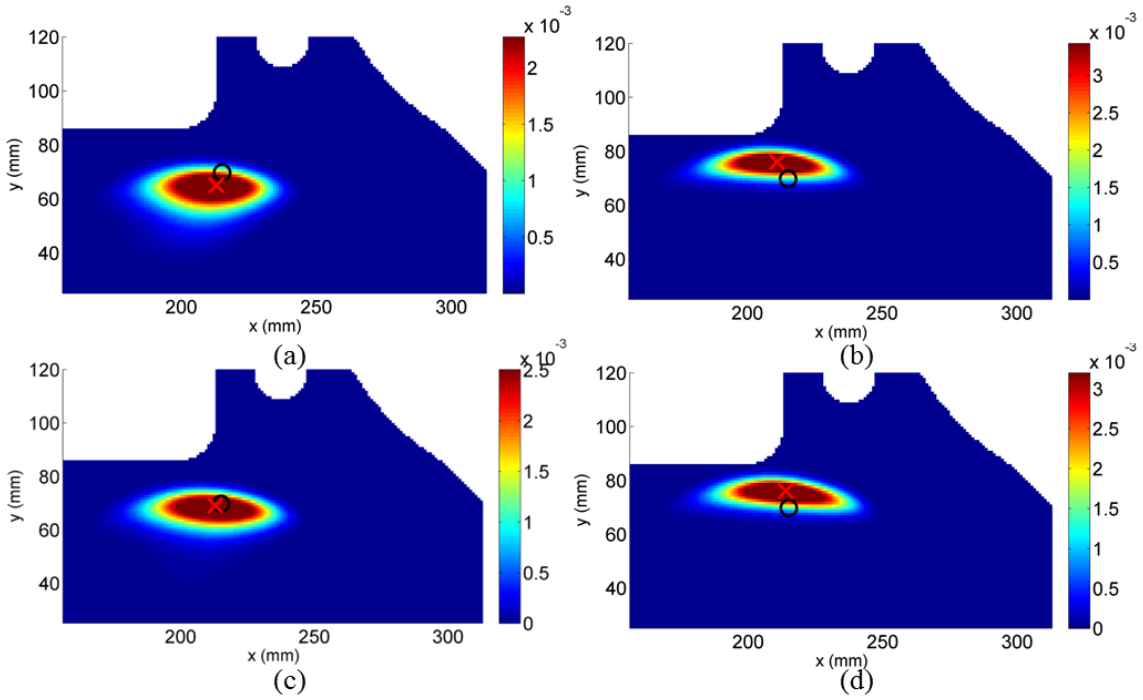

Figure 3.9. 20°C (a), 40°C (b), 60°C (c), and 80°C (d) localizations for cycle 90,417 with o denoting true damage location and x as estimated damage location.

The localization for the 20.6 mm crack at 90,417 cycles can be seen in Figure 3.9. This figure shows a similar trend as before, where the localization error decreases as the crack tip moves from the boundary of the lug joint. Another important result to observe is the decrease in the variance of the damage likelihood distribution.

The localization error at four different temperatures in the lug joint experiments using the temperature and velocity estimation algorithm can be seen in Table 3.3.

Table 3.3. Localization error in lug joint fatigue test using velocity estimation.

Cycles	20°C		40°C		60°C		80°C	
	(x,y) (mm)	**Error (mm)**	**(x,y) (mm)**	**Error (mm)**	**(x,y) (mm)**	**Error (mm)**	**(x,y) (mm)**	**Error (mm)**
81,761	(212,87)	4.64	(210,78)	8.80	(210,70)	16.61	(212,72)	15.12
85,537	(216,67)	20.11	(210,83)	3.27	(212,76)	10.27	(212,74)	12.11
86,106	(212,74)	11.23	(210,71)	13.69	(209,76)	8.61	(209,67)	17.60
86,248	(209,83)	0.31	(214,67)	17.04	(214,71)	13.27	(210,75)	8.36
86,889	(209,81)	1.63	(219,68)	16.89	(210,65)	17.29	(215,70)	13.27
87,737	(212,71)	10.37	(209,86)	5.00	(209,67)	14.37	(212,72)	9.38
88,208	(207,86)	7.16	(212,67)	13.62	(214,66)	14.79	(212,78)	2.63
88,819	(216,66)	13.19	(210,74)	5.28	(212,64)	14.7	(211,72)	6.84
89,247	(210,77)	3.00	(211,66)	11.57	(214,85)	7.67	(213,73)	4.40
89,557	(213,70)	5.83	(210,79)	4.96	(213,66)	9.80	(211,73)	3.92
89,794	(212,76)	2.87	(210,66)	9.22	(215,68)	6.24	(216,73)	2.13
90,076	(216,65)	7.47	(210,72)	4.39	(208,76)	7.38	(213,68)	4.51
90,417	(213,65)	5.15	(211,76)	7.53	(213,69)	2.23	(214,76)	6.41

Table 3.3 confirms the trend shown before of decreasing error as crack length increases. This reduction is due to the ability of the algorithm to more accurately select the damage reflected time-of-flight as it becomes significantly different from a boundary-reflected time-of-flight. Even with the larger localization error at smaller crack lengths, the average localization errors were 7.15 mm, 9.33 mm, 11.02 mm, and 8.21 mm for 20°C, 40°C, 60°C, and 80°C respectively.

3.3.4. Comparison of Estimated and Fixed Velocity Damage Localization Results

To show that using the temperature and velocity estimation algorithm improves damage localization results, the damage localization results from the velocity estimated case must be compared against localization results when the velocity is fixed. Assuming there is no information on the temperature a structure is interrogated at, a common assumption may be to use the room temperature wave velocity. Damage localization

performance for 89,557 cycles at temperatures of 20°C, 40°C, 60°C, and 80°C using a fixed room temperature velocity of 3,065 m/s can be seen in Figure 3.10.

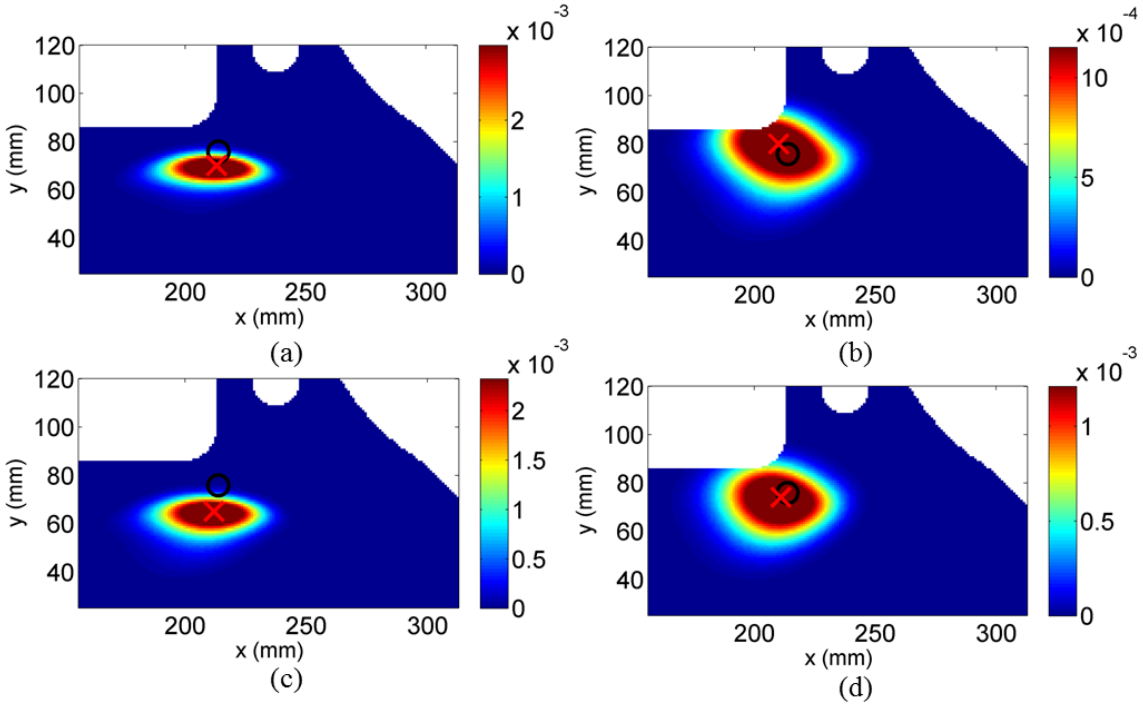

Figure 3.10. 20°C (a), 40°C (b), 60°C (c), and 80°C (d) localizations for cycle 89,557 using room temperature velocity with o denoting true damage location and x as estimated damage location.

Figure 3.10 shows that there is mixed performance when using a fixed room temperature velocity for localization at an unknown temperature. Comparing the localization results in Figure 3.10 to the results when using the estimated velocity, the localization error was found to be constant when the estimated velocity is used for 20°C, decrease by 0.70 mm for 40°C and 1.11 mm for 60°C, and increase by 0.63 mm for 80°C. The likely reason for the small improvement in localization error is that the maximum difference between the room temperature and actual velocities is approximately 30 m/s, which would produce a smaller error than the error from the time-of-flight measurements.

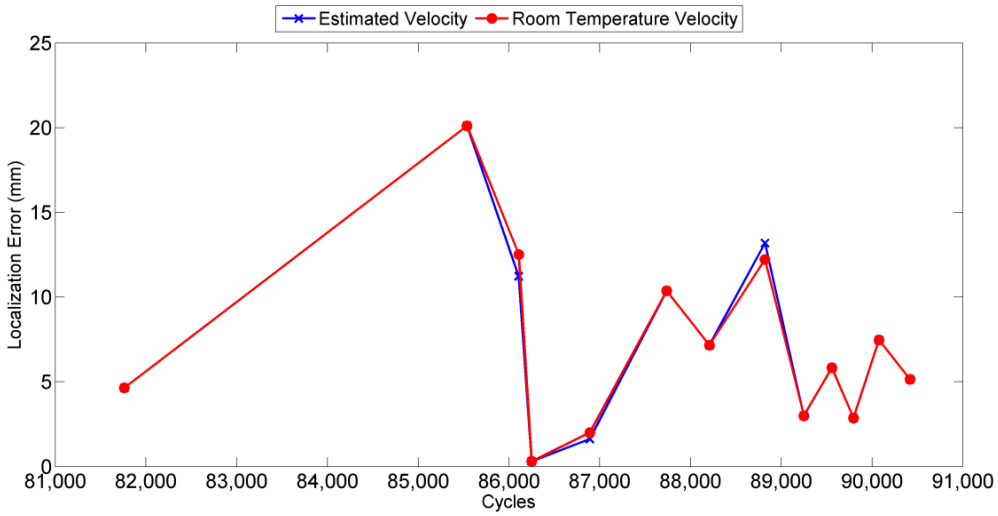

Figure 3.11. Estimated velocity and room temperature velocity localization error for 20°C.

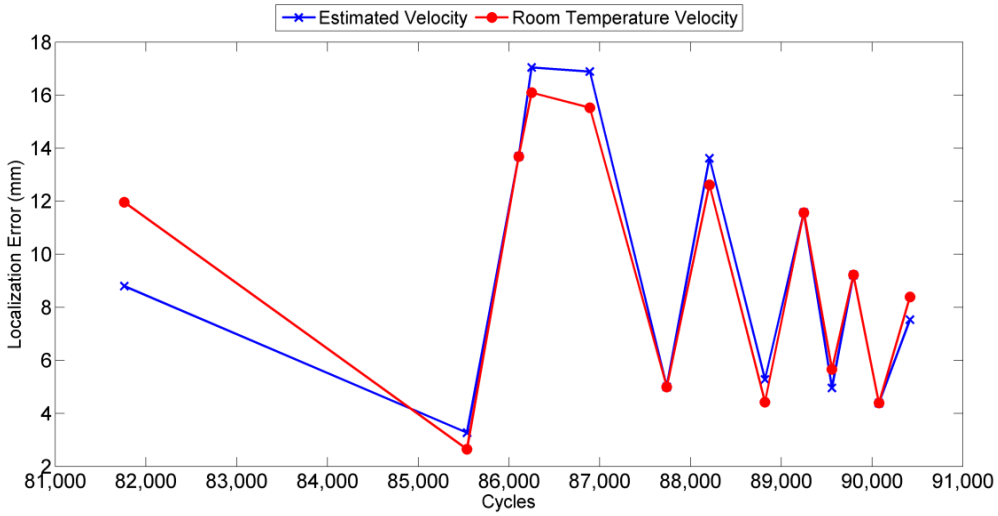

Figure 3.12. Estimated velocity and room temperature velocity localization error for 40°C.

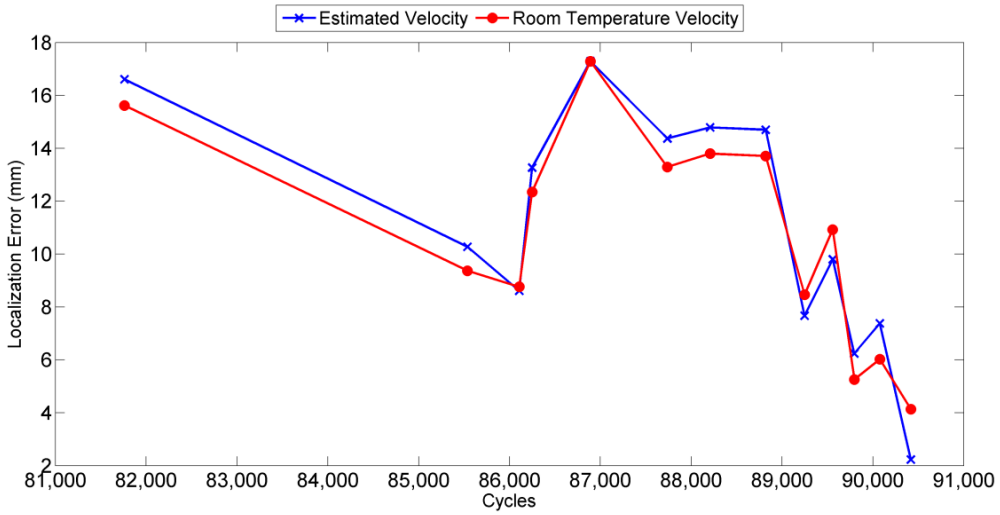

Figure 3.13. Estimated velocity and room temperature velocity localization error for 60°C.

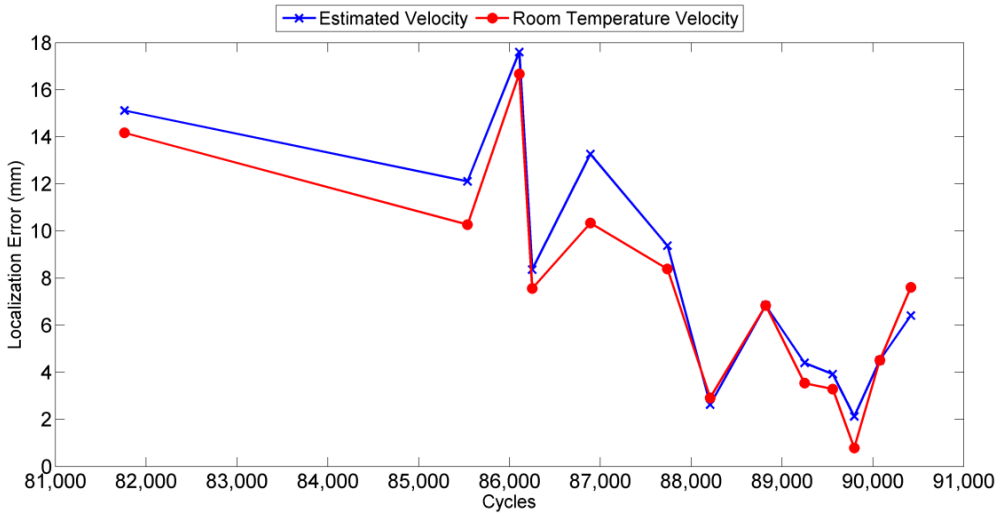

Figure 3.14. Estimated velocity and room temperature velocity localization error for 80°C.

Figure 3.11 through Figure 3.14 show a comparison of the localization error when using the estimated or the fixed room temperature velocity. These figures show that using the estimated velocity instead of the room temperature velocity did not make a significant impact on the localization error. Using the estimated velocity, the average localization error was found to decrease by 0.06 mm for 20°C, and increase by 0.01 mm for 40°C, 0.33 mm

for 60°C, and 0.75 mm for 80°C. The likely reason for the lack of localization error improvement when using the estimated velocity is that the velocity difference of approximately 30 m/s between 20°C and 80°C is minimal compared to the error associated with the time-of-flight measurements. If the damage were localized at higher temperatures, using the estimated velocity would provide more accurate localization results because the error associated with the velocity difference would become greater than the measurement error.

3.4. Numerical Modeling for Algorithm Validation at Extreme Temperatures

To validate the localization algorithm at a wider range of temperatures, the 3D electromechanical coupled elastodynamic local interaction simulation approach/sharp interface model (EMC LISA/SIM) presented in [62] was used. The EMC LISA/SIM model allows for the determination of the time-varying displacement field and electric potential of a piezoelectric transducer in an arbitrary geometry model. The EMC LISA/SIM approach solves the mechanical equations of motion as an initial value problem and Maxwell's equation as a boundary value problem for each time step. The EMC LISA/SIM model has also been shown to be computationally more efficient than available finite element methods for wave propagation [62-65].

The general procedure for solving the 3D uncoupled elastodynamic wave equation using LISA/SIM was first developed by Delsanto [65]. The elastodynamic LISA/SIM allows for a domain to be discretized into cuboidal elements of size Δx, Δy, Δz. Material properties are applied as a constant to each cell, but can vary between cells. The sharp interface model (SIM) allows for the exact treatment of nodes that are shared by cells with different material properties which allows waves to propagate across sharp material

boundaries [64]. The EMC LISA/SIM technique solves the piezoelectric constitutive equations, the elastodynamic wave equation, and Maxwell's equation using a combination of a central difference scheme and an enforcement of tractions and electric displacement across the element interfaces [62].

3.4.1. Electromechanical Coupled LISA/SIM Implementation

The lug joint model was created using a rectangular domain of size 324 mm x 150 mm in the x-y plane, meshed with 1 mm x 1 mm square elements. The z-direction was discretized into 13 layers, with each layer corresponding to $1/6^{th}$ of the lug joint's thickness or approximately 1.06 mm. These dimensions of the domain ensured that a minimum of three layers of air were present around the lug joint to ensure convergence of the model [62]. Figure 3.15 shows the lug joint model at the top surface of the lug joint.

Figure 3.15. Lug joint domain used in EMC LISA/SIM.

The areas represented by white in Figure 3.15 correspond to the regions where aluminum materials properties are applied, while the blue area represents regions assigned the material properties of air. The fatigue crack that was modeled in EMC LISA/SIM corresponds to the fatigue crack found in the experimental tests at 90,417 cycles. The

fatigue crack path was modeled using position measurements from calibrated images using digital image measurement tools. The material properties of air were assigned along the crack path to model the presence of the crack. The piezoelectric elements used were modeled as 1 mm x 1 mm square elements and were placed in the z-direction on the layer above the aluminum properties. The material properties used for the piezoelectric elements were found in [61].

The range of temperatures investigated using the EMC LISA/SIM were from -60°C to 150°C and were selected based upon the expected operating temperature range of a guided wave SHM system using piezoelectric transducers. In order to model the effects of temperature, the material properties of the aluminum were varied according to *E*-temperature data provided in MIL-HDBK-5 [60]. The piezoelectric material properties were held constant over the temperature range because temperature effects on the piezoelectric materials were not considered to produce first-order errors in damage localization. Also, the temperatures investigated were below half of the PZT Curie temperature so no polarization effects were expected to occur in the PZT material.

In order to minimize the amount of numerical error due to pulse distortion, the Courant Friedrich Lewy (CFL) number was satisfied for all simulations. The CFL number is represented by

$$CFL = c_{\max}\Delta t\sqrt{\frac{1}{\Delta x^2}+\frac{1}{\Delta y^2}+\frac{1}{\Delta z^2}} \le 1, \tag{3.6}$$

where c_{max} is the longitudinal wave speed, Δt is the sampling frequency, and Δx, Δy, Δz correspond to the size of the elements [66]. In order to keep the CFL number constant and near 1 while keeping the element size fixed, the sampling period must be varied to

compensate for changes in the longitudinal wave speed due to the changing material properties. In this investigation a CFL number of 0.9972 was used for all simulations.

3.4.2. EMC LISA/SIM Numerical Results

Before the temperature and damage estimations can be compared, the mean shift in the time-of-flight measurements must be calculated as done in Section 2.2.1 to ensure the time-of-flight measurements follow the assumed wave velocity model. The mean shift was defined as the difference between the theoretical time-of-flight and the measured time-of-flight in an undamaged lug joint using the EMC LISA/SIM model. The mean shifts from the EMC LISA/SIM model can be seen in Table 3.4.

Table 3.4. Mean time shift for EMC LISA/SIM model.

Sensor Path	**Mean Shift, δ (μs)**
2-5, 3-6	4.3
1-5, 3-7	-4.1
2-4, 4-6	0.0
1-4, 4-7	2.9

The same time-of-flight measurement standard deviations from the experimental data were used for the EMC LISA/SIM.

The first output of the proposed algorithm that must be compared between the experimental and numerical results is the estimated temperature. The estimated temperature must be correct in the EMC LISA/SIM model or the damage localization results will not compare with the experimental results. A comparison between the temperature estimation results from the EMC LISA/SIM and the experiments can be seen in Figure 3.16.

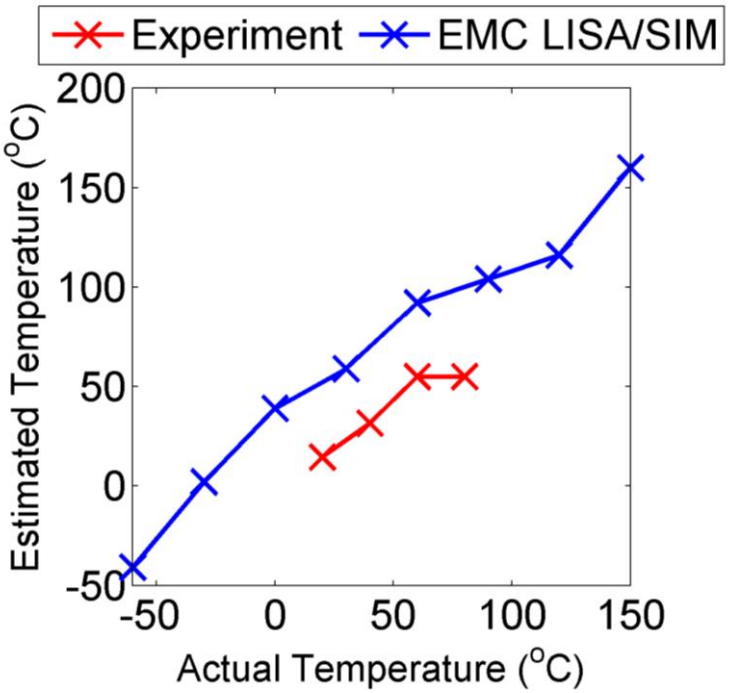

Figure 3.16. Comparison of estimated temperatures from EMC LISA/SIM and experiments.

Figure 3.16 shows that the temperatures from the EMC LISA/SIM results were overestimated compared to the experimental results. A likely cause for the difference is human error in the positioning of the PZTs in the experiment. Another possible cause of error is in the modeling of the crack. The element size used was a 1 mm x 1 mm square, so the crack is wider than in the experiments and does not have the exact same path. These differences in the crack modeling may have influenced the stress field in the EMC LISA/SIM model and caused the velocity error.

The relationship between the estimated and actual temperatures for the EMC LISA/SIM results in Figure 3.16 appears to be linear. While there is the large shift in the estimated temperature error, the error is approximately constant. This shows that the temperature-velocity algorithm can be used at a wider range of temperatures than what was

tested experimentally. The error shift could be compensated for with a more detailed modeling of the lug joint used in the experiments. This includes refining the mesh size, creating a more representative crack path, and using the actual material properties rather than the nominal material properties listed in MIL-HDBK-5.

The damage localization error for the EMC LISA/SIM results can be seen in Table 3.5.

Table 3.5. Damage localization error using EMC LISA/SIM.

Temperature (°C)	**(x,y) (mm)**	**Error (mm)**
-60	(216,73)	3.16
-30	(213,76)	6.32
0	(208,81)	13.04
30	(213,76)	6.32
60	(215,74)	4.00
90	(212,76)	6.71
120	(215,74)	4.00
150	(210,81)	12.08

The results in Table 3.5 show an average localization error of less than 7 mm, which is similar to what was seen in the experimental results. The localization error tends to be between 4 mm and 6 mm, but there are two large increases in error at 0°C and 150°C. The large increases in error are likely due to the error in the temperature estimation. This error directly causes the incorrect selection of wave velocity, which can greatly affect the localization results. A typical damage localization result can be seen in Figure 3.17.

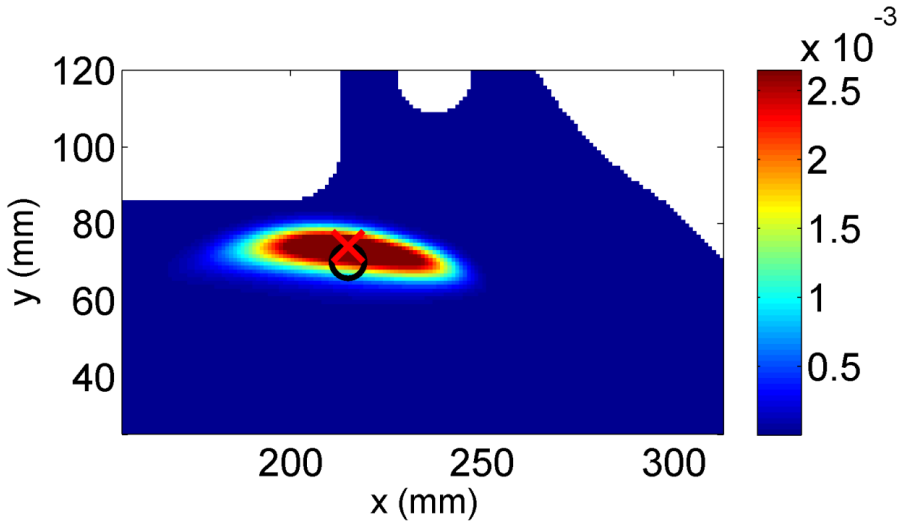

Figure 3.17. Damage localization for 60°C EMC LISA/SIM model with o denoting true damage location and x as estimated damage location.

Figure 3.17 shows that the results from the EMC LISA/SIM model are similar in their means and variances to those from the experimental results. The estimated high probability regions from EMC LISA/SIM have the same characteristic shape as the high probability regions found in the experiments.

A comparison between the localization error when using a fixed room temperature velocity, and the estimated velocity with the EMC LISA/SIM results, can be seen in Figure 3.18.

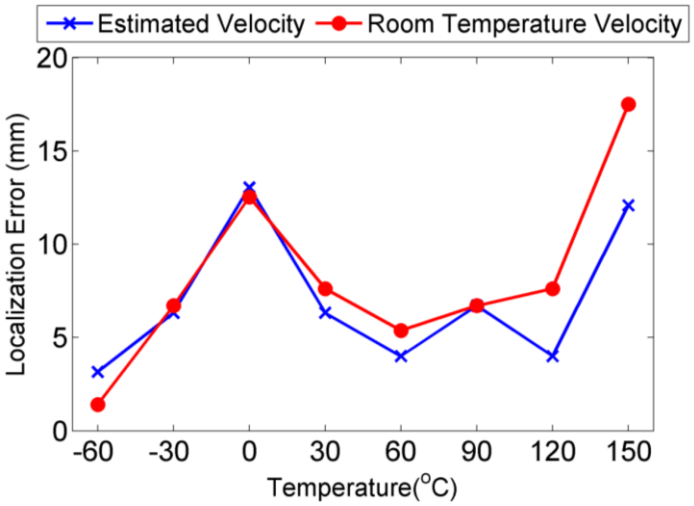

Figure 3.18. Comparison of localization error at different temperatures using EMC LISA/SIM results.

The results in Figure 3.18 show that using the estimated velocity improved the localization error in the majority of the temperatures investigated. Use of the estimated velocities had the largest impact on the localization error at temperatures above 120°C. This result is expected, because as temperature increases the errors from incorrectly selecting the velocity will begin to outweigh the time-of-flight measurement errors. The average decrease in localization error was found to be 1.23 mm.

By comparing the similarity in the temperature estimation trend, damage localization error, and damage posterior distribution shape, the EMC LISA/SIM model has been shown to yield representative results of those found in experiments. The results from EMC LISA/SIM have shown that the probabilistic damage localization algorithm using temperature and velocity estimation is capable of accurately predicting, adapting, and localizing damage for the entire temperature range in which a guided wave SHM system can be operated.

3.5. Concluding Remarks

A novel approach was presented that incorporated temperature and velocity estimation with probabilistic damage localization. The temperature and velocity estimation algorithm used *in situ* wave signals and a numerically calculated velocity-temperature dictionary in order to estimate the temperature and wave speed in a structure. This estimated wave speed was then used in the damage localization algorithm to make the algorithm independent of any parameters that may change as a function of temperature. The proposed approach was verified both experimentally and numerically, this was done to ensure the algorithm could function throughout the operating temperature range of a PZT guided wave localization system.

Experimentally, the temperature estimation algorithm was found to estimate temperature very accurately. For temperatures less than 70°C, the mean temperature of the experimental distribution was found to be less than 4°C from the actual temperature. Above 70°C the temperature estimation error increased, likely due to temperature effects on the adhesive, sensor wiring, or DAQ. The temperature estimation results were confirmed using the EMC LISA/SIM model. The model found a linear trend with a constant error offset when comparing the estimated and actual temperatures. By creating a more representative lug joint model the offset error is expected to reduce. Because the estimation error is constant, a linear shift can be used to compensate for the offset. By accounting for this offset the temperature estimation algorithm can be used across the entire operating temperature range of a PZT localization system.

The experimental results from the fatigued lug joint test demonstrated excellent correlation with the true values. The largest difference between the estimated and the

theoretical wave speeds was found to be 0.807%, which corresponds to a velocity difference of 25 m/s. Using the estimated velocities, the average localization error was found to be 7.15 mm, 9.33 mm, 11.02 mm, and 8.21 mm for 20°C, 40°C, 60°C, and 80°C respectively. Comparing the localization error of when the estimated velocity was used to the localization error of when the room temperature velocity was used showed little change in the experimental results. The minimal impact of using the estimated velocity is likely due to the small temperature difference in the experimental tests. The small temperature difference corresponded to roughly a 30 m/s velocity difference, which would produce smaller errors than the errors associated with the time-of-flight measurements. When the estimated velocity was used in the EMC LISA/SIM results the localization error was found to decrease for the majority of the localization results. Using the estimated velocity decreased the localization error on average by 1.23 mm. The velocity and temperature estimation can be extended to estimate the temperature along each sensor path. By estimating the temperature along each sensor path structures with large thermal gradients can have improved damage localization performance.

Chapter 4

SUMMARY AND FUTURE DIRECTIONS

This research focused on developing a novel probabilistic approach to localize damage in metallic structures at unknown temperatures using guided waves. A modified time-frequency analysis signal processing technique, called Grouped Matching Pursuit Decomposition, has been used. This methodology allows for a more accurate estimation for the time-of-flight of a dispersive signal using computationally simple atoms. Next, a probabilistic framework was presented that combines prior knowledge on the damage location from finite element analysis with information from noisy time-of-flight measurements. The probabilistic method also incorporated probabilistic data association to account for uncertainties in time-of-flight measurement origin, and allows the entire localization algorithm to operate in an unsupervised manner. Experiments were conducted to verify the algorithm. An aluminum lug joint was used as the test article. The lug joint was subjected to fatigue loading between 1.3 kN and13 kN and the resulting crack was localized at room temperature. The probabilistic method was shown to provide a good indication of damage location over a range of crack lengths. The localization error increased as crack lengths reduced below 4 mm. Small crack lengths and crack tips near boundaries were found to have large localization error due to error in the time-of-flight measurements from multiple waves arriving at a similar time. However, the localization approach was shown to be capable of placing a region of high probability around the true damage location at larger crack lengths without any user input.

Once the probabilistic localization algorithm was shown to perform well at room temperature, the algorithm was extended to localize damage at unknown temperatures. A

model was created using the theoretical dispersion curves to define a relationship between the temperature and the wave speed. Various methods were presented on how to incorporate a probabilistic estimate of the wave velocity in the localization algorithm using *in situ* signals. The proposed algorithm was then verified experimentally and numerically using the aluminum lug joint. The proposed temperature estimation algorithm was experimentally shown to accurately predict the temperature of a structure between 20°C and 70°C. Numerically, the estimated temperature range was extended from -60°C to 150°C using the EMC LISA/SIM model. Use of the estimated velocities in damage localization for the experimental results did not provide any significant impact on the localization error. No measureable change in performance was observed because the time-of-flight measurement error was greater than the error that resulted from using the incorrect velocity at the temperatures tested. When validated numerically the use of the estimated velocity at temperatures above 120°C was shown to increase localization performance.

To summarize, an unsupervised and temperature-independent probabilistic framework has been developed for damage localization in metallic structures. Although results were demonstrated on aluminum lug joints, the methodology can be extended and applied to many other material systems. With further research, the isotropic velocity propagation model could be modified to allow the algorithm to be used in anisotropic materials. Also, different damage sensitive parameters, such as chirp rate or signal amplitude, can easily be included in the probabilistic framework to aid in localization. With the use of the association events and a numerical wave propagation model the probabilistic data association algorithm can even be used to detect the presence of damage. To improve velocity estimation, the temperature and velocity can be measured along each sensor path

independently. Estimating the temperature along each sensor path would allow for more accurate characterization of the temperature distribution across a structure subjected to a strong thermal gradient. The extension that would provide the most potential for this algorithm is the inclusion of a physics-based damage evolution model. Using a damage evolution model would allow the prior knowledge to be updated dynamically to a predicted damage location. This would result in more accurate localization results with a smaller variance.

REFERENCES

[1] Shull, P.J., *Nondestructive Evaluation: Theory, Technique and Applications*, CRC Press, 2002.

[2] Coelho, C.K., Kim, S.B., and Chattopadhyay, A., "Optimal Sensor Placement for Active Guided Wave Interrogation of Complex Metallic Components," *Proceedings of SPIE*, vol. 7981, no. 79813O, 2011.

[3] Raghavan, A., and Cesnik, C.E.S., "Review of Guided-Wave Structural Health Monitoring," *Shock Vib.*, vol. 39, no. 2, 2007, 91-114.

[4] Lynch, J.P., and Loh, K.J., "A Summary Review of Wireless Sensors and Sensor Networks for Structural Health Monitoring," *Shock Vib.*, vol. 38, no. 2, 2006, 91-128.

[5] Lamb, H., "On Waves in an Elastic Plate," *Proc. Roy. Soc. London, Ser. A*, vol. 93, no. 648, 1917, 114-128.

[6] Graff, K.F., *Wave Motion in Elastic Solids*, Columbus, OH: Ohio State University Press, 1975.

[7] Soni, S., "Structural Health Management of Aerospace Hotspots Under Fatigue Loading," *PhD Dissertation*, Arizona State University, 2010.

[8] Michaels, J.E., "Effectiveness of In Situ Damage Localization Methods using Sparse Ultrasonic Sensor Arrays," *Proceedings of SPIE*, vol. 6935, no. 6935-35, 2008.

[9] Ihn, J.B. and Chang, F.K., "Pitch-Catch Active Sensing Methods in Structural Health Monitoring for Aircraft Structures," *Struct. Health Monit.*, vol. 7, no. 1, 2008, 5-19.

[10] Lee, S.J., Gandhi, N., Hall, J.S., Michaels, J.E., Xu, B., Michaels, T.E., and Ruzzene, M., "Baseline-Free Guided Wave Imaging via Adaptive Source Removal," *Struct. Health Monit.*, vol. 11, no. 4, 2012, 472-481.

[11] Levine, R.M., Michaels, J.E., and Lee, S.J., "Boundary Reflection Compensation in Guided Wave Baseline-Free Imaging," *AIP Conference Proceedings*, vol. 1335, 2011, 113-120.

[12] Flynn, E.B., Todd, M.D., Wilcox, P.D., Drinkwater, B.W., and Croxford, A.J., "Maximum-Likelihood Estimation of Damage Location in Guided-Wave Structural Health Monitoring," *Proc. R. Soc. A*, vol. 467, no. 2133, 2011, 2575-2596.

[13] Todd, M.D., Flynn, E.B., Wilcox, P.D., Drinkwater, B.W., Croxford, A.J., and Kessler, S., "Ultrasonic Wave-Based Defect Localization Using Probabilistic Modeling," *AIP Conference Proceedings*, vol. 1430, 2012, 639-646.

[14] Zhou, C., Su, Z., and Cheng, L., "Probability-Based Diagnostic Imaging using Hybrid Features Extracted from Ultrasonic Lamb Wave Signals," *Smart Mater. Struct.*, vol. 20, no. 12, 2011.

[15] Zhou, C., Su, Z., and Cheng, L., "Quantitative Evaluation of Orientation-Specific Damage using Elastic Waves and Probability-Based Diagnostic Imaging," *Mech. Syst. Signal Pr.*, vol. 25, no. 6, 2011, 2135-2156.

[16] Su, Z., Wang, X., Cheng, L., Yu, L., and Chen, Z., "On Selection of Data Fusion Schemers for Structural Damage Evaluation," *Struct. Health Monit.*, vol. 8, no. 3, 2009, 223-241.

[17] Yu, L., and Su, Z., "Application of Kernel Density Estimation in Lamb Wave-Based Damage Detection," *Math. Probl. Eng.*, vol. 2012, no. 406521, 2012.

[18] Niri, E.D., and Salamone, S., "A Probabilistic Framework for Acoustic Emission Source Localization in Plate-Like Structures," *Smart Mater. Struct.*, vol. 21, no. 3, 2012.

[19] Niri, E.D., Salamone, S., and Singla, P., "Acoustic Emission (AE) Source Localization using Extended Kalman Filter (EKF)," *Proceedings of SPIE*, vol. 8348, no. 834804, 2012.

[20] Niri, E.D., Farhidzadeh, A., and Salamone, A., "Adaptive Multisensor Data Fusion for Acoustic Emission Source Localization in Noisy Environment," *Struct. Health Monit.*, vol. 12, no. 1, 2013, 59-77.

[21] Yan, G., "A Bayesian Approach for Damage Localization in Plate-Like Structures using Lamb Waves," *Smart Mater. Struct.*, vol. 22, no. 3, 2013.

[22] Couch, L.W., *Digital and Analog Communication Systems*, 6th edition, Prentice Hall, 2001.

[23] Demirli, R., "Model Based Estimation of Ultrasonic Echoes: Analysis, Algorithms, and Applications," *PhD Dissertation*, Illinois Institute of Technology, 2001.

[24] Xu, B., Yu, L., and Giurgiutiu, "Lamb Wave Dispersion Compensation in Piezoelectric Wafer Active Sensor Phased-Array Applications," *Proceedings of SPIE*, vol. 7295, no. 729516, 2009.

[25] Mallat, S.G., and Zhang, Z., "Matching Pursuits with Time-Frequency Dictionaries," *IEEE T. Signal Proces.*, vol. 41, no. 12, 1993, 3397-3415.

[26] Xu, B., Yu, L., Giurgiutiu, V., "Advanced Methods for Time-of-Flight Estimation with Application to Lamb Wave Structural Health Monitoring," in *The 7th International Workshop of Structural Health Monitoring*, 2009.

[27] Kishimoto, K., Inoue, H., Hamada, M., and Shibuya, Y., "Time Frequency Analysis of Dispersive Waves by Means of Wavelet Transform," *J. Appl. Mech.*, vol. 62, no. 4, 1995, 841-846.

[28] La Saponara, V., Lestari, W., Winkelmann, C., Arronche, L., and Tang, H.Y., "Fatigue Damage Identification in Composite Structures Through Ultrasonics and Wavelet Transform Signal Processing," *AIP Conference Proceedings*, vol. 1335, 2011, 927-934.

[29] Lu, Y., Ye, L., Su, Z., "Crack Identification in Aluminium Plates Using Lamb Wave Signals of a PZT Sensor Network," *Smart Mater. Struct.*, vol. 15, no. 3, 2006, 839-849.

[30] Bagheri, A., Li, K., and Rizzo, P., "Reference-Free Damage Detection by Means of Wavelet Transform and Empirical Mode Decomposition Applied to Lamb Waves," *J. Intel. Mat. Syst. Str.*, vol. 24, no. 2, 2013, 194-208.

[31] Xu, B., Giurgiutiu, and Yu, L., "Lamb Waves Decomposition and Mode Identification Using Matching Pursuit Method," *Proceedings of SPIE*, vol. 7292, no. 729101-1, 2009.

[32] Lu, Y., and Michaels, J.E., "Feature Extraction and Sensor Fusion for Ultrasonic Structural Health Monitoring Under Changing Environmental Conditions," *Sensors Journal IEEE*, vol. 9, no. 11, 2009, 1462-1471.

[33] Lu, Y., and Michaels, J.E., "Numerical Implementation of Matching Pursuit for the Analysis of Complex Ultrasonic Signals," *IEEE T. Ultrason. Ferr.*, vol. 55, no. 1, 2008, 173-182.

[34] Soni, S., Kim, S.B., and Chattopadhyay, A., "Fatigue Crack Detection and Localization using Reference-Free Method," *Proceedings of SPIE*, vol. 7648, no. 76480U-1, 2010.

[35] Kim, S.B., Chattopadhyay, A., and Nguyen, A.D., "The Use of Matching Pursuit Decomposition for Damage Detection and Localization in Complex Structures," *Proceedings of SPIE*, vol. 7981, no. 798129-1, 2011.

[36] Das, S., Papandreou-Suppappola, A., Zhou, X., and Chattopadhyay, A., "On the use of the Matching Pursuit Decomposition Signal Processing Technique for Structural Health Monitoring," *Proceedings of SPIE*, vol. 5764, no. 583, 2005.

[37] Okopal, G., and Loughlin, P.J., "Dispersion-Invariant Features for Classification," *J. Acoust. Soc. Am.*, vol. 123, no. 2, 2008, 832-841.

[38] Okopal, G., and Loughlin, P., "Feature Extraction for Classification of Signal Propagating in Channels with Dispersion and Dissipation," *Proceedings of SPIE*, vol. 6566, no. 65660G-1, 2007.

[39] Wilcox, P., "A Rapid Signal Processing Technique to Remove the Effect of Dispersion from Guided Wave Signals," *IEEE T. Ultrason. Ferr.*, vol. 50, no. 4, 2003, 419-427.

[40] Sohn, H., Park, H.W., Law, K.H., and Farrar, C.R., "Combination of a Time Reversal Process and a Consecutive Outlier Analysis for Baseline-free Damage Diagnosis," *J. Intel. Mat. Syst. Str.*, vol. 18, no. 4, 2007, 335-346.

[41] Gangadharan, R., Murthy, C.R.L., Gopalakrishnan, S., and Bhat, M.R., "Time Reversal Technique for Health Monitoring of Metallic Structures Using Lamb Waves," *Ultrasonics*, vol. 49, no. 8, 2009, 696-705.

[42] Hoseini, M.R., Wang, X., and Zuo, M.J., "Estimating Ultrasonic Time of Flight Using Envelope and Quasi Maximum Likelihood Method for Damage Detection and Assessment," *Measurement*, vol. 45, no. 8, 2012, 2072-2080.

[43] Flynn, E.B., Todd, M.D., Croxford, A.J., Drinkwater, B.W., and Wilcox, P.D., "Enhanced Detection Through Low-Order Stochastic Modeling for Guided-Wave Structural Health Monitoring," *Struct. Health Monit.*, vol. 11, no. 2, 2012, 149-160.

[44] Francis, P.H., "Thermo-Mechanical Effects in Elastic Wave Propagation: A Survey," *J. Sound Vib.*, vol. 21, no. 2, 1972, 181-192.

[45] Gandhi, N., and Michaels, J.E., "Efficient Perturbation Analysis of Lamb Wave Dispersion Curves," *AIP Conference Proceedings*, vol. 1211, 2010, 215-222.

[46] Raghavan, A., and Cesnik, C.E.S., "Effects of Elevated Temperature on Guided-Wave Structural Health Monitoring," *J. Intel. Mat. Syst. Str.*, vol. 19, no. 12, 2008, 1383-1398.

[47] Croxford, A.J., Moll, J., Wilcox, P.D., and Michaels, J.E., "Efficient Temperature Compensation Strategies for Guided Wave Structural Health Monitoring," *Ultrasonics*, vol. 50, no. 4-5, 2010, 517-528.

[48] Lu, Y., and Michaels, J.E., "A Methodology for Structural Health Monitoring with Diffuse Ultrasonic Waves in the Presence of Temperature Variations," *Ultrasonics*, vol. 43, no. 9, 2005, 717-731.

[49] Moll, J., Fritzen, C.P., "Guided Waves for Autonomous Online Identification of Structural Defects Under Ambient Temperature Variations," *J. Sound Vib.*, vol. 331, no. 20, 2012, 4587-4597.

[50] Clarke, T., and Cawley, P., "Enhancing the Defect Localization Capability of a Guided Wave SHM System Applied to a Complex Structure." *Struct. Health Monit.*, vol. 10, no. 3, 2010, 247-259.

[51] Konstantinidis, G., Wilcox, P.D., and Drinkwater, B.W., "An Investigation Into the Temperature Stability of a Guided Wave Structural Health Monitoring System Using Permanently Attached Sensors," *Sensors Journal IEEE*, vol.7, no. 5, 2007, 905-912.

[52] Moll, J., Heftrich, C., and Fritzen, C.P., "A Rapid and Velocity-Independent Damage Localization Approach for Ultrasonic Structural Health Monitoring," *IEEE T. Ultrason. Ferr.*, vol. 59, no. 6, 2012, 1309-1315.

[53] Bar-Shalom, Y. and Tse, E., "Tracking in a Cluttered Environment With Probabilistic Data Association," *Automatica*, vol. 11, 1975, 451-460.

[54] Bar-Shalom, Y., Daum, F., and Huang, J., "The Probabilistic Data Association Filter," *IEEE Contr. Syst. Mag.*, vol. 29, no. 6, 2009, 82-100.

[55] Bar-Shalom, Y., Chang, K.C., and Blom, H.A.P., "Automatic Track Formation in Clutter with a Recursive Algorithm," *IEEE Proc. 28th Conf. Dec. Control*, 1989, 1402-1408.

[56] Papandreou-Suppappola, A., *Applications in Time-Frequency Signal Processing*, Florida: CRC Press, 2002.

[57] Trees, H.L.V., *Detection, Estimation, and Modulation Theory, Part I*, Wiley Interscience, 2001.

[58] Duda, R.O., Hart, P.E., and Stork, D.G., *Pattern Classification*, 2nd ed., Wiley Interscience, 2001.

[59] MacKay, D.J.C., *Information Theory, Inference, and Learning Algorithms*, Cambridge University Press, 2003.

[60] United States Department of Defense, *MIL-HDBK-5J*, 2003.

[61] APC International, "Physical and Piezoelectric Properties of APC Materials", Retrieved from http://www.americanpiezo.com/apc-materials/piezoelectric-properties.html, n.d.

[62] Borkowski, L., Liu, K.C., and Chattopadhyay, A., "Fully Coupled Electromechanical Elastodynamic Model for Guided Wave Propagation Analysis," *J. Intel. Mat. Syst. Str.*, In Press.

[63] Delsanto, P.P., Whitcombe, T., Chaskelis, H.H., and Mignogna, R.B., "Connection Machine Simulation of Ultrasonics Wave Propagation in Materials I: One-Dimensional Case," *Wave Motion*, vol. 16, no. 1, 1992, 65-80.

[64] Delsanto, P.P., Schechter, R.S., Chaskelis, H.H., Mignogna, R.B., and Kline, R., "Connection Machine Simulation of Ultrasonics Wave Propagation in Materials II: Two-Dimensional Case," *Wave Motion*, vol. 20, no. 4, 1994, 295-314.

[65] Delsanto, P.P., Schechter, R.S., and Mignogna, R.B., "Connection Machine Simulation of Ultrasonics Wave Propagation in Materials III: Three-Dimensional Case," *Wave Motion*, vol. 26, no. 4, 1997, 329-339.

[66] Virieux, J., "P-SV Wave Propagation in Heterogeneous Media: Velocity Stress Finite Difference Method," *Geophysics*, vol. 51, no. 4, 1986, 889-901.